Journal of Polymers and the Environment (2026) 34:160
https://doi.org/10.1007/s10924-026-03830-6

ORIGINAL PAPER

Water-Based Electrospun HC/PVA/CA Nanofibers for Wound Healing Applications: A Sustainable Strategy for Cell-Proliferative and Antibacterial Functionality

Elçin Tören[1,2] · **Jakub Wiener**[1]

Received: 25 October 2025 / Accepted: 3 April 2026 / Published online: 16 June 2026
© The Author(s) 2026

Abstract

This study presents an eco-friendly approach for developing advanced wound-dressing materials composed of hydrolyzed collagen (HC), poly(vinyl alcohol) (PVA), and a triterpene-rich extract from Centella asiatica (CA). HC/PVA nanofibers were fabricated via needle-free electrospinning using water as a green solvent, followed by glutaraldehyde vapour crosslinking. The incorporation of CA extract (1–7% w/v) significantly influenced fiber morphology and biological functionality. Comprehensive characterization, including SEM, FTIR, rheological analysis, and mechanical testing, revealed systematic modifications of the polymer matrix properties with CA integration. Mechanical testing demonstrated optimal performance at 3% CA, with a tensile strength of 4.82 ± 0.34 MPa and Young's modulus of 142.5 ± 12.3 MPa. In vitro cell studies demonstrated that 1–3% CA concentrations significantly enhanced fibroblast adhesion and proliferation (with a 142.3 ± 8.5% increase in viability at day 7) as well as collagen synthesis (a 238.5 ± 15.2% increase relative to the control). Antibacterial disc diffusion tests demonstrated effective inhibition of Staphylococcus aureus (14.2 ± 1.1 mm at 5% CA) and Escherichia coli (12.8 ± 0.9 mm at 5% CA). These results indicate that HC/PVA/CA nanofibers represent a sustainable multifunctional platform for advanced wound care applications.

Keywords Electrospinning · Hydrolysed collagen · Poly(vinyl alcohol) · *Centella asiatica* · Wound healing

Introduction

The skin constitutes approximately 16% of body weight and spans an area of 1.8 to 2.0 square meters in the average adult. It is the largest organ and one of the most complex organs [1]. This barrier maintains homeostasis and protects the body from external threats, including physical trauma, chemicals, and microorganisms. The skin comprises three primary layers: the epidermis, dermis, and hypodermis [2]. The Epidermis, predominantly consisting of keratinocytes, serves as the initial defence, preventing dehydration and blocking pathogen entry. Beneath the Epidermis lies the dermis, which is abundant in collagen and elastin fibers, conferring strength and elasticity to the skin. The hypodermis, characterised by a high concentration of adipose and connective tissues, serves as an energy reserve, providing insulation to the body and absorbing mechanical shock [3].

In addition to its protective function, the skin plays crucial roles in thermoregulation, sensory perception, vitamin D synthesis, and immune surveillance. These functions are crucial for maintaining the physiological homeostasis. When the skin is compromised due to trauma, burns, surgical interventions, or conditions such as diabetes or vascular disorders, the body initiates a complex healing process [4]. This process occurs in four distinct phases: hemostasis, inflammation, proliferation, and remodelling [5]. Figure 1 illustrates the progression of these phases, highlighting the key cellular and molecular mechanisms involved in skin repair.

Given its multifunctional nature, even minor disruptions in the skin structure can significantly impair its protective role [3]. Damage to this environment typically initiates a

✉ Elçin Tören
elcin.toren@tul.cz

[1] Faculty of Textile Engineering, Technical University of Liberec, 1402/2, Liberec 461 17, Czech Republic

[2] NANOVACZECH s.r.o., Příkop, 843/4, Brno 602 00, Czech Republic

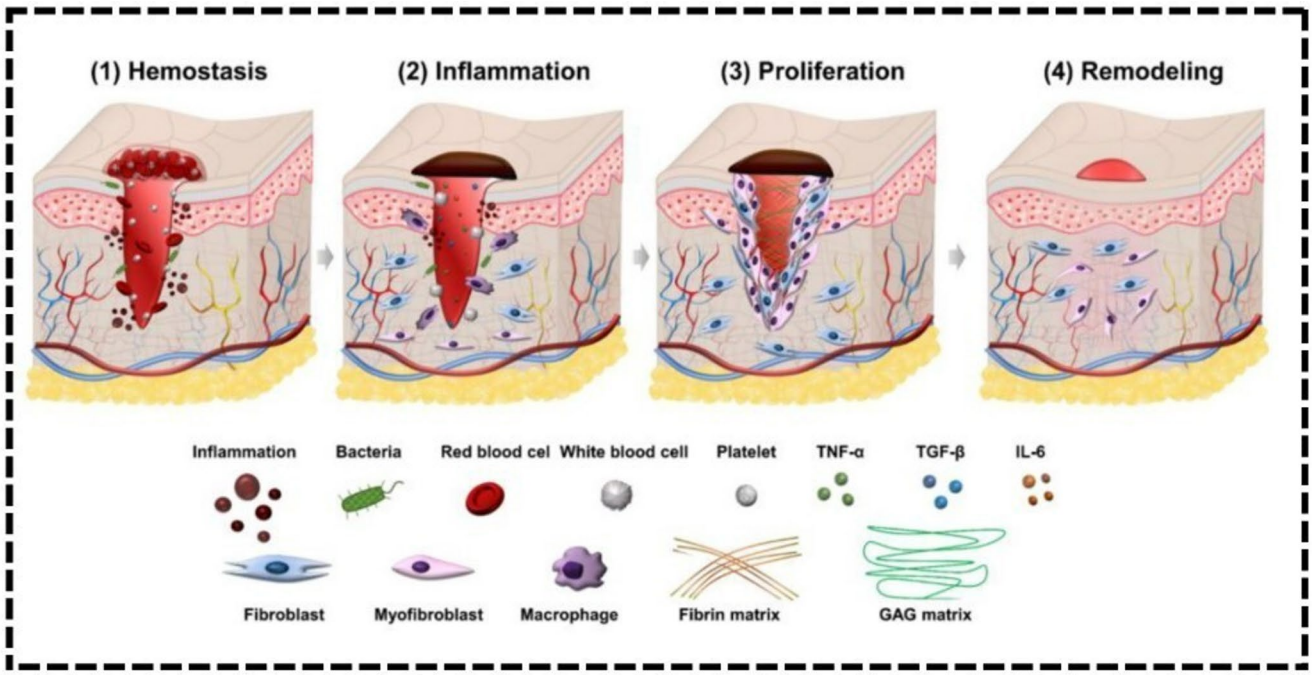


Fig. 1 Schematic representation of the four sequential and overlapping phases of the wound healing process [6]. (1) Hemostasis: Immediate vasoconstriction and clot formation. (2) Inflammation: Recruitment of macrophages and neutrophils to eliminate debris and bacteria. (3) Proliferation: fibroblast activation, collagen deposition, and granulation tissue formation. (4) Remodelling – reorganisation of collagen fibres and restoration of tissue integrity

series of biologically regulated processes that constitute the wound healing response [7].

Chronic wounds represent a critical global healthcare challenge, affecting approximately 40 million people annually and imposing treatment costs of over 25 billion USD [8]. These persistent injuries, frequently associated with diabetes, vascular disorders, and aging populations, lead to prolonged suffering and diminished Quality of Life (QoL), while creating substantial socioeconomic burdens [9]. Traditional wound dressings, such as gauze, cotton pads, and basic hydrocolloids, provide passive protection by maintaining moisture but do not actively participate in tissue regeneration [10]. Their fundamental limitations include the absence of antimicrobial activity, insufficient oxygen permeability, and inability to deliver bioactive cues that stimulate angiogenesis, collagen synthesis, and cellular proliferation, which are essential for complete wound closure [10, 11]. Chronic wounds represent a significant burden to global healthcare systems, affecting millions of patients annually and incurring substantial economic costs estimated at over $25 billion in the United States. The complexity of wound healing, involving overlapping phases of hemostasis, inflammation, proliferation, and remodelling, necessitates advanced therapeutic strategies that can simultaneously address multiple pathological factors. Traditional wound dressings often fail to provide the multifunctional properties required for adequate healing, particularly in cases complicated by bacterial infections and impaired cellular regeneration. Consequently, there is an urgent need for innovative biomaterial platforms that can promote cell proliferation while preventing microbial colonization.

Nanofiber-based wound dressings have emerged as promising platforms owing to their high surface area-to-volume ratio, tunable porosity, and structural similarity to the native extracellular matrix (ECM), which enables enhanced cell adhesion and proliferation [10, 12]. Recent advances in sustainable wound care materials have explored various strategies to minimize environmental impact while maintaining their therapeutic functionality [13]. Ahmad et al. reported that the multiple jet formation used in needleless electrospinning systems significantly increased the production yield and that the resulting nanofibers showed high morphological homogeneity with a narrower diameter distribution [14]. Khan et al. developed reduced graphene oxide/arabinoxylan/chitosan composites with pH-sensitive antibacterial activity for wound dressing applications, demonstrating responsive antimicrobial behaviour in acidic wound environments. Similarly, chitosan/poly(vinyl alcohol)/graphene oxide hydrogel films exhibited controlled antimicrobial release and enhanced cell viability, with reports indicating up to 85% bacterial inhibition against *S. aureus* and *E. coli* while maintaining 90% fibroblast viability after 72 h [15]. Ali et al. fabricated electrospun polycaprolactone/gelatin nanofibers loaded with curcumin and ZnO nanoparticles,

achieving accelerated wound closure in diabetic rat models; however, they required dimethylformamide as the primary solvent [16]. Augustine et al. developed electrospun PCL membranes incorporating biosynthesised silver nanoparticles, which demonstrated antibacterial efficacy against wound pathogens; however, this approach raised concerns about silver accumulation and potential cytotoxic effects at elevated concentrations [17].

Despite these technological advancements, persistent concerns have arisen regarding synthetic additives, metal-organic frameworks, and graphene-based nanomaterials, specifically their long-term environmental persistence, potential metal ion leaching, cytotoxic effects on mammalian cells at elevated concentrations, and energy-intensive production requirements [18]. Graphene oxide synthesis typically involves harsh oxidising agents such as potassium permanganate and concentrated sulfuric acid, generating hazardous chemical waste [19]. Furthermore, the incomplete removal of organic solvents from electrospun scaffolds poses significant challenges; residual dimethylformamide levels as low as 100 ppm have been shown to induce hepatotoxicity and developmental abnormalities [20]. Recent studies have also emphasized that organic solvents used in electrospinning not only increase environmental burden but may negatively influence membrane biocompatibility, whereas water-based electrospinning offers a safer and more sustainable alternative [21].

Bibliometric analysis revealed that citations related to "green nanofibers wound healing" increased from 2 in 2015 to 26 in 2025, reflecting the growing recognition of sustainability imperatives in biomaterial development. However, "hydrolysed collagen nanofibers" remain critically underexplored, with only nine publications in the past decade, highlighting a significant research gap despite collagen's well-established role in tissue regeneration [22]. Hydrolyzed collagen (HC), derived from the controlled enzymatic degradation of native collagen using proteases such as pepsin or bacterial collagenase, offers distinct advantages, including low molecular weight (typically 2–10 kDa), complete water solubility, superior processability, and enhanced cell affinity through exposed bioactive peptide sequences, including Gly Pro-Hyp triplets that promote integrin-mediated cell adhesion [23]. Unlike native collagen, which requires acidic solvents for dissolution, HC's water solubility of HC eliminates the need for organic solvents during electrospinning, addressing a primary environmental concern. Moreover, HC retains the critical biological activities of native collagen, including stimulation of fibroblast migration and proliferation through activation of the PI3K/Akt signalling pathway, upregulation of matrix metalloproteinase-2 expression, which facilitates ECM remodelling, and provision of amino acid building blocks for de novo collagen synthesis [24].

Centella asiatica (CA), a medicinal herb with centuries of traditional use documented in Ayurvedic and Traditional Chinese Medicine, contains pentacyclic triterpene compounds, including asiaticoside (30–40% of total triterpenes), madecassoside (20–30%), asiatic acid (15–25%), and madecassic acid (10–20%), which collectively stimulate fibroblast proliferation, enhance collagen synthesis, promote angiogenesis, and exhibit antimicrobial and anti-inflammatory activities [25]. Mechanistically, asiaticoside activates the TGF-β1/Smad2/3 signalling cascade, inducing the expression of collagen type I (COL1A1) and type III (COL3A1) genes by 2.5-fold and 2.8-fold, respectively, in human dermal fibroblasts, as demonstrated by quantitative PCR analysis [26]. Asiatic acid enhances wound angiogenesis by upregulating VEGF and activating endothelial nitric oxide synthase (eNOS), resulting in increased microvessel density [27]. The antibacterial mechanisms of CA triterpenes involve disruption of bacterial cell membrane integrity, interference with quorum-sensing systems that regulate biofilm formation, and inhibition of bacterial protein synthesis [28]. Importantly, CA extract represents a renewable botanical resource obtained through environmentally benign aqueous or ethanol extraction processes, thereby avoiding energy-intensive synthesis (typically requiring temperatures exceeding 1000 °C and multi-step chemical reactions) and potential environmental persistence associated with graphene derivatives or metal-based antimicrobial agents. Life cycle assessment studies indicate that the production of botanical extracts generates approximately 85% fewer carbon emissions than the synthesis of silver nanoparticles [29].

When combined with PVA's mechanical reinforcement of PVA (tensile strength: 25–45 MPa) and superior electrospinnability, characterized by solution optimization, the HC/PVA/CA system presents an unprecedented opportunity to develop completely water-based, bioactive nanofiber platforms that are simultaneously therapeutically effective and environmentally responsible [30]. Recent studies have also demonstrated that PVA-based electrospun membranes exhibit excellent mechanical stability, high hydrophilicity, and favorable biocompatibility, making PVA an effective structural component in biomedical nanofiber systems [31].PVA facilitates fiber formation through the entanglement of its linear polymer chains and provides structural integrity through extensive hydrogen bonding networks. The synergistic interaction between HC's bioactivity of HC, PVA's mechanical properties of PVA, and CA's therapeutic compounds of CA creates a multifunctional scaffold that addresses the complex, multifaceted requirements of wound healing while adhering to green chemistry principles, including waste prevention, the use of renewable feedstocks, and design for degradation [32].Recent studies

on electrospun PVA-based hybrid nanofibers have further demonstrated that combining PVA with natural polysaccharides such as alginate and cellulose significantly improves structural stability, water-retention behavior, and the capacity to encapsulate and protect bioactive agents, highlighting the relevance of PVA-containing biopolymer systems for advanced biomedical delivery applications [33].

This study aimed to develop and comprehensively characterize green-synthesized HC/PVA/CA nanofiber membranes for advanced wound-healing applications. The novelty of this study lies in the following aspects: (1) complete elimination of toxic organic solvents through water-based needleless electrospinning; (2) incorporation of hydrolyzed collagen, which has rarely been explored in electrospun nanofiber form despite its superior water solubility and bioactivity; (3) integration of *Centella asiatica* extract as a renewable bioactive agent, circumventing the need for synthetic pharmaceuticals or metal-based additives; (4) systematic optimization of CA concentration (1–7% w/v) to balance cell-proliferative and antibacterial functionalities; and (5) glutaraldehyde vapor-phase crosslinking, which minimizes reagent consumption and eliminates liquid waste compared to conventional combining the intrinsic bioactivity of collagen hydrolysate with a nanofibrous ECM-mimicking architecture and CA's therapeutic properties would yield a sustainable, nontoxic wound dressing capable of enhancing fibroblast proliferation, stimulating collagen synthesis, providing antimicrobial protection, and maintaining controlled degradation. This study advances environmentally conscious biomedical materials by demonstrating that green chemistry principles can be successfully integrated with clinical effectiveness, offering a scalable platform aligned with circular economy concepts in healthcare biomaterials.

Materials and Methods

Materials

Hydrolyzed collagen (Peptan® B 2000 LD) was obtained from Rousselot (Rousselot, Chassieu, France). It contains short peptide chains with an average molecular weight of approximately 2 kDa, a protein content of at least 90%, and a viscosity of 2 to 4 mPa Â ·s at 20% (w/v) in water (pH 5.0 to 6.5). Poly(vinyl alcohol)PVA (Mw = 89,000–98,000 Da, 99+% hydrolyzed, semicrystalline) was obtained from Sigma-Aldrich (Czech Republic). Centella asiatica extract (PMQD0802, Plamed Green Science Group Co., Ltd., Xi'an, China) contained 10% total triterpenes, including asiaticoside, madecassoside, asiatic acid, and madecassic acid. Glutaraldehyde (GA; 25% aqueous solution) acted as a bifunctional aldehyde crosslinker and was purchased from Sigma-Aldrich (Czech Republic). NIH-3T3 mouse embryonic fibroblast cells were provided by SVEN Bioblast (USA) for experiments on cytocompatibility and collagen synthesis. Dulbecco's modified Eagle's medium (DMEM), fetal bovine serum (FBS), and penicillin-streptomycin were obtained from the Gibco (Grand Island, NY, USA). The Sircol™ Soluble Collagen Assay Kit (Biocolor Ltd., Belfast, UK) was used for quantitative measurement of soluble collagen using the Sirius Red dye-binding method.

Methods

Preparation of HC Solution

HC was dissolved in distilled water at various concentrations (20%, 25%, and 30% w/v) under continuous magnetic stirring for 6 h at room temperature (25 ± 2 °C) and relative humidity of approximately 40% until a homogeneous and transparent solution was obtained.

Preparation of HC / PVA Solution

HC/PVA was dissolved in distilled water to obtain a total polymer concentration of 30% (w/v), and HC provided a uniform fiber morphology during electrospinning. This was due to the high density of the hydroxyl, carboxyl, and amide functional groups. These groups increase the hydrogen bonding interactions and molecular entanglement with the PVA chains. As a result, these interactions improve the solution viscosity, electrostatic charge distribution, and jet stability. This led to smoother, bead-free fibres. HC and PVA were blended at weight ratios of 70:30, 60:40, and 50:50 (w/w) to investigate the effect of composition on fibre formation. The mixtures were magnetically stirred for 6 h at room temperature (25 ± 2 °C) and relative humidity of approximately 40% until homogeneous and transparent solutions were obtained. Distilled water was used as a green solvent for preparing the HC/PVA polymeric solution. This highlighted the use of distilled water as an eco-friendly solvent and the creation of uniform polymer solutions before electrospinning.

Preparation of HC / PVA / CA Solution

HC and PVA were separately dissolved in distilled water to create a 30% (w/v) polymer stock solution. The solutions were mixed at a weight ratio of HC/PVA = 60/40 (w/w) and magnetically stirred for 6 h at room temperature (25 ± 2 °C, RH = 40%) until a uniform mixture was formed. CA was added to the HC/PVA blend at concentrations of 1–7% (w/v) based on the total polymer content. Seven formulations were prepared before electrospinning. The addition of CA

was optimised to ensure a good balance between bioactivity and electrospinnability while also preventing phase separation at higher concentrations.

Electrospinning Process

All prepared polymer solutions were electrospun using a needle-free electrospinning system (NUENEX, Respilon Nanofibers, Czech Republic), as shown in Fig. 2, under controlled laboratory conditions of 25 ± 2 °C and 40 ± 2% relative humidity. The polymer solutions were placed in the open reservoir of a rotating cylindrical electrode, and nanofibers were formed under a high-voltage electric field. We optimised the process parameters, including the applied voltage, distance from the electrode to the collector, and rotation speed, to achieve uniform fibre deposition. The optimal electrospinning conditions were established at an applied voltage of 45 kV, a distance of 18 cm between the electrode and collector, and a rotation speed of 3 rpm. The nanofibrous mats were dried at room temperature for 24 h and stored in a desiccator until further characterisation.

Glutaraldehyde (GA) Vapour Crosslinking Process

Electrospun nanofiber membranes were crosslinked under controlled conditions using glutaraldehyde (GA) vapour. This process ensures structural stability while reducing potential cytotoxicity. A 25% (w/w) aqueous GA solution (10 mL) was placed in a 35 × 10 mm glass dish at the bottom of a 2 L sealed desiccator. Nanofiber mats were suspended on the upper support grid. The system was maintained at a temperature of 25 ± 2 °C for 12 h, allowing the GA vapor to diffuse and gradually achieve uniform crosslinking throughout the nanofiber matrix. Subsequently, the samples were aerated for 2 h and rinsed three times with deionized water to remove any unreacted GA. The samples were then dried in a ventilated oven at 40 °C for 24 h to ensure that all solvents had evaporated and could be handled safely for biological testing.



Fig. 2 Needle-free electrospinning

Scanning Electron Microscopy (SEM)

The surface morphology of the electrospun HC/PVA nanofibers containing CA extract was examined using a Phenom ProX scanning electron microscope (Thermo Fisher Scientific, Netherlands) operated at an accelerating voltage of 10 kV in high vacuum mode. SEM micrographs were acquired at a magnification of 10,000× for fiber diameter analyses. Fibre diameters were measured from the images using ImageJ software (version 1.53, NIH, USA), with at least 100 randomly selected, non-overlapping fibres measured per formulation. The mean fiber diameter, standard deviation, and diameter distribution histograms were calculated using GraphPad Prism software. Prior to imaging, the nanofiber samples were coated with a 10 nm gold layer using a Phenom Coater to improve their surface conductivity and reduce the charging effects during imaging.

Fourier transform infrared (FTIR)

Fourier transform infrared (FTIR) spectra of the electrospun nanofiber mats were recorded to identify the key functional groups in the HC, PVA, and CA components. The recordings were also intended to confirm the presence of possible intermolecular interactions between the molecules. Spectral analysis was conducted using a Nicolet iZ10 FTIR spectrometer (Thermo Fisher Scientific, USA). This device has a diamond-attenuated total reflectance (ATR) accessory. We collected spectra in the range of 4000 to 500 cm^{-1} with a spectral resolution of 4 cm^{-1}, averaging each spectrum over 32 scans.

Rheological Characterisation

The rheological properties of the electrospinning solutions were comprehensively characterized to understand their processability and predict fiber formation behavior. Viscosity measurements were performed using a rotational viscometer (Brookfield DV-II + Pro, Middleboro, MA, USA) equipped with spindle number 4 (suitable for viscosity range 200–8000 cP). The measurements were conducted at 25 ± 0.1 °C using a temperature-controlled water bath. The spindle was immersed in 50 mL of the sample solution and rotated at a shear rate of 60 rpm. Viscosity readings were recorded after allowing 3 min for equilibration, and three measurements were taken for each sample at 1-minute intervals. The viscosity values were calculated automatically using the instrument software and expressed in centipoise (cP). The electrical conductivity was measured using a benchtop

conductivity meter (Mettler Toledo Seven Compact S213, Switzerland) equipped with a temperature compensation probe at 25 °C. The probe was immersed in 30 mL of solution, and readings were taken after stabilization (typically 30–60 s). Three measurements were performed for each sample, and the results were expressed in microsiemens per centimeter (μS/cm). The surface tension was determined using the pendant drop method with an optical contact angle goniometer (DataPhysics OCA 15EC, Germany). A drop of solution (approximately 8 μL) was formed at the tip of the needle using a precision syringe pump, and the drop profile was captured using a high-resolution CCD camera. Five measurements were performed per sample at 25 °C, and the results were expressed in millinewtons per meter (mN/m). All rheological measurements were performed in triplicate, and the data are presented as mean ± standard deviation.

Mechanical Properties

The tensile properties were measured using a universal testing machine (Instron 5544, USA) equipped with a 100 N load cell, in accordance with ASTM D882-12. Rectangular specimens (50 mm × 10 mm) were cut from the nanofiber mats and conditioned at 25 ± 2 °C and 65 ± 2% RH for 24 h. The tests were performed at a crosshead speed of 30 mm/min with a gauge length of 10 mm until failure. The tensile strength (maximum stress, MPa), Young's modulus (slope of the initial linear region, MPa), and elongation at break (%) were calculated from the stress-strain curves. Five specimens per sample were tested, and the results are reported as mean ± SD. Statistical significance was assessed using one-way ANOVA with Tukey's post-hoc test ($p < 0.05$).

Water retention

CA-loaded HC/PVA (60/40, w/w) nanofiber membranes containing 1–7% (w/v) CA extract (10% total triterpenes) were electrospun for 4 h under the optimised conditions.The water retention study was performed as a short-term swelling analysis. The wet weight (Wt) was measured immediately after gentle surface blotting without drying, in order to determine the fluid uptake capacity rather than degradation behavior.

After electrospinning, the nanofiber mats were crosslinked using glutaraldehyde (GA) vapour to improve their structural stability. A 25% aqueous GA solution was carefully dispensed into a 35 mm ×10 mm glass dish placed at the bottom of a sealed desiccator, and the nanofiber membranes were positioned on the upper platform. The setup was maintained at room temperature (25 ± 2 °C) for 12 h to allow for gradual vapor diffusion and homogeneous crosslinking within the nanofiber matrix.

Following crosslinking, the membranes were transferred to a well-ventilated drying oven and maintained at 40 °C for 48 h to ensure the complete removal of unreacted GA residues.

For the water-retention assay, 3 mg samples of the dried nanofiber membranes were immersed in 1 mL of distilled water for time-dependent measurements. To assess the influence of environmental pH, the same procedure was performed using PBS buffer at pH 7.4 (physiological condition) and additional test solutions adjusted to pH 5.4 (acidic wound environment) and pH 9.0 (alkaline stress condition).

$$Water\ retention\ (\%) = \frac{W_t - W_i}{W_i} \times 100 \quad (1)$$

Where *Wi* is the initial weight of the specimen in its dry state, and *Wt* is the weight of the specimen after submersion in distilled water for a given length of time.

Weight loss

Nanofiber membranes composed of CA-loaded HC/PVA (60/40, w/w) containing 7% (w/v) CA extract (containing 10% total triterpenes) were produced via electrospinning for 4 h under optimized conditions. To evaluate the degradation behavior, approximately 3 mg of each dried nanofiber membrane was immersed in 1 mL of distilled water and phosphate-buffered saline (PBS, pH 7.4) and incubated at room temperature for 1, 4, 7, 14, and 21 days. The samples were carefully removed, gently blotted with filter paper to eliminate surface moisture, air-dried at 40 °C, and weighed. Subsequently, the samples were lyophilized to ensure complete removal of residual moisture prior to the final measurement.Subsequently, the samples were lyophilised to ensure complete removal of residual moisture prior to the final measurement. The percentage weight loss was calculated using Eq. (2).

$$Weight\ loss\ (\%) = \frac{W_i - W_d}{W_i} \times 100 \quad (2)$$

Cell Analysis

In Vitro Cytocompatibility Evaluation

NIH-3T3 mouse embryonic fibroblast cells were utilised to evaluate the cytotoxic, adhesive, and proliferative properties of the HC/PVA/CA nanofiber membranes, in accordance with the ISO 10993-5:2009 guidelines. Since NIH-3T3 is a widely available continuous cell line, no additional ethical approval was required. To investigate the dose-dependent effects on the cell response, seven formulations were prepared by incorporating 1–7% (w/v) CA extract into the

HC/PVA (60/40, w/w) blend. Prior to biological testing, all nanofiber membranes were crosslinked with glutaraldehyde (GA) vapour under controlled conditions to enhance their structural integrity. Thereafter, the membranes were thoroughly washed with Phosphate-Buffered Saline (pH 7.4) to ensure the removal of residual GA. The crosslinked and PBS-treated membranes were subsequently used in all cytocompatibility experiments.

The sterilization process involved the use of ultraviolet (UV) light, and the samples (20 mm in diameter) were exposed for 30 min. Subsequently, the samples were immersed in PBS (pH 7.4) for 10 h. This was performed to ensure the complete removal of any residual glutaraldehyde and to ascertain the biocompatibility of the samples prior to cell seeding. NIH-3T3 fibroblasts were seeded at a density of 1×10^4 cells per well in 24-well tissue culture plates containing Dulbecco's modified Eagle's medium (DMEM) supplemented with 10% (v/v) fetal bovine serum (FBS) and 1% (v/v) penicillin-streptomycin. Cell cultures were maintained for 48 h at 37 °C in a humidified incubator supplied with 5% CO_2 atmosphere.

After incubation, cell morphology and attachment were examined using a scanning electron microscope (Phenom ProX, Thermo Fisher Scientific, Netherlands). SEM images revealed that the fibroblast cells were evenly distributed and securely attached to the CA-enriched nanofiber surfaces, exhibiting the normal spindle-like shape characteristic of healthy fibroblasts.

The MTT assay was used to evaluate cell viability after a 48-hour incubation. A microplate reader was used to measure the optical density (OD) at 570 nm.

Cell Culture

NIH-3T3 mouse embryonic fibroblast cells were cultivated in Dulbecco's Modified Eagle Medium (DMEM) with 10% (v/v) fetal bovine serum (FBS) and 1% (v/v) penicillin-streptomycin (50 $U \cdot mL^{-1}$). The cells were maintained at 37 °C in a humidified incubator with 5% CO_2 atmosphere to facilitate growth and proliferation. The culture medium was changed at 48-hour intervals to maintain optimal nutrient levels and prevent pH imbalances.

When the cells reached approximately 80–90% confluence, they were detached using 0.25% (w/v) trypsin-EDTA solution. The solution was neutralised with fresh DMEM containing FBS, followed by centrifugation at 1000 rpm for 5 min. The cell pellet was resuspended in a complete growth medium and used to seed the nanofiber membranes and perform cell viability tests.

Cell Seeding and Proliferation

NIH-3T3 fibroblasts were seeded onto crosslinked HC/PVA/CA nanofiber scaffolds, which were placed in 24-well culture plates at an initial density of 5×104 cells/well. The control group was comprised of crosslinked HC/PVA membranes devoid of CA. The cultures were maintained at 37 °C in a humidified atmosphere containing 5% CO_2, and the culture medium was replaced every 48 h to ensure an adequate nutrient supply and removal of metabolic waste products.

The number of metabolically active cells adhered to the scaffold surface was determined using the MTT assay after incubation for 1, 2, 3, and 4 days. At each designated time point, the culture medium was replaced with a 0.5 mg/mL MTT solution and incubated for 4 h at 37 °C. The resulting purple formazan crystals were dissolved in 500 µL of dimethyl sulfoxide (DMSO) per well. Optical density (OD) was measured at 570 nm using a microplate reader. The relative cell viability of the samples was calculated in comparison to fibroblasts cultured on pristine crosslinked HC/PVA membranes, which served as the control group.

Samples were collected after a 72-hour incubation period to evaluate cell morphology and surface attachment. The cells were fixed with 10% (v/v) neutral-buffered formalin for 20 min, dehydrated using a graded ethanol series (75%, 80%, 90%, 99%, and 100%), and lyophilised. The dried specimens were sputter-coated with a thin layer of gold and examined under a scanning electron microscope (SEM; Phenom ProX, Thermo Fisher Scientific, Netherlands).

Collagen Synthesis Activity of Fibroblasts

The in vitro collagen synthesis activity of fibroblasts cultured on HC/PVA/CA nanofiber membranes was evaluated to determine the bioactive influence of CA incorporation on extracellular matrix (ECM) formation. The assay quantified the extent to which triterpenes released from the nanofibrous scaffolds stimulated de novo collagen production by NIH-3T3 fibroblasts.

Electrospun HC/PVA (60/40, w/w) nanofiber membranes containing 3% and 5% (w/v) CA extract were used as test substrates, while pristine HC/PVA membranes served as controls. Circular specimens (20 mm in diameter) were sterilised with UV light for 30 min and immersed in PBS (pH 7.4) for 10 h to eliminate residual GA and soluble impurities. The membranes were placed in 24-well plates, and NIH-3T3 fibroblasts were seeded at a density of 1×10^4 cells per well in DMEM supplemented with 10% FBS and 1% penicillin–streptomycin. Cultures were maintained at 37 °C under 5% CO_2 and 95% relative humidity.

After 24 h and 72 h of incubation, the culture supernatants were collected to quantify newly synthesised soluble

collagen. Collagen concentration was determined using the Sircol™ Soluble Collagen Assay Kit according to the manufacturer's instructions. Briefly, the supernatant was mixed with Sirius Red dye reagent and incubated for 30 min at room temperature to form a collagen–dye complex. The complex was centrifuged, washed to remove the unbound dye, and resolubilised in an alkaline reagent. Optical density (OD) was measured at 540 nm using a microplate reader.

The relative collagen synthesis rate (%) was calculated with respect to the control group according to Eq. (3):

$$Collagen\ synthesis\ (\%) = \frac{A_{sample}}{A_{control}} \times 100 \quad (3)$$

Where A_{sample} denotes the absorbance of fibroblasts cultured on HC/PVA (60/40, w/w) nanofiber membranes containing **3–5% (w/v)** *CA* extract, and $A_{control}$corresponds to fibroblasts cultured on pristine crosslinked HC/PVA membranes without CA.

Antibacterial Activity

The antibacterial efficacy of the electrospun HC/PVA/CA nanofiber membranes was evaluated using the agar diffusion plate method, in accordance with ISO 20645:2019(E), a standard test procedure for antibacterial textile fabrics. The test was performed against both *Gram-positive* (*Staphylococcus aureus (14.2 ± 1.1 mm at 5% CA)*, ATCC 12600) and *Gram-negative* (*Escherichia coli (12.8 ± 0.9 mm at 5% CA)*, ATCC 11229) bacterial strains to assess the inhibitory activity of CA-enriched nanofibers.

Sterile Mueller–Hinton agar (MHA) plates with a uniform thickness of approximately 3 mm were prepared and inoculated with freshly cultured bacterial suspensions adjusted to approximately 1.5×10^8 colony-forming units per millilitre ($CFU \cdot mL^{-1}$), corresponding to the 0.5 McFarland turbidity standard. Circular nanofiber membrane samples (20 mm in diameter) of the crosslinked PVA, HC/PVA, and HC/PVA/CA formulations were sterilised under UV light for 30 min and aseptically placed on the surface of the inoculated agar.

A gentamicin disc (10 µg) was used as a positive control, whereas a pristine crosslinked HC/PVA membrane served as a negative control. The plates were then incubated at 37 °C for 24 h under aerobic conditions. After incubation, the bacterial inhibition zones around each sample were observed and measured using a digital Vernier calliper with an accuracy of ± 0.01 mm. The antibacterial activity index (A) was calculated using Eq. (4).

$$A = \frac{(D-d)}{2} \quad (4)$$

Where D is the diameter of the total inhibition zone (mm), and d is the specimen diameter (20 mm). A higher value corresponds to greater antibacterial performance, indicating more effective diffusion of active triterpenoid compounds from the nanofibrous matrix into the agar medium.

Wettability (Contact Angle)

The surface wettability of the nanofiber membranes was determined by static water contact angle measurements using the sessile drop technique (OCA 15EC, DataPhysics Instruments, Germany). Prior to testing, the samples were conditioned at 25 ± 2 °C and 50 ± 5% relative humidity for 24 h. A 5 µL droplet of distilled water was deposited onto the membrane surface using an automated microsyringe to ensure precise volume control. The droplet image was captured within 5 s of deposition to avoid evaporation effects, and the contact angle was calculated by fitting the droplet profile with the Young–Laplace equation using the instrument software. For each formulation, measurements were performed at three different locations on three independent samples ($n = 3$), and the results are reported as mean ± standard deviation (SD).

Results and Discussion

SEM Analysis

The surface morphologies of the hydrolyzed collagen (HC) nanofibers prepared from aqueous solutions with varying concentrations (20, 25, and 30% w/v) are shown in Fig. 3. At a concentration of 20% (w/v), the nanofibers exhibited continuous but irregular structures with local thickening, indicating that the viscosity affected the electrospinning jet stability and fiber formation dynamics. Increasing the concentration to 25% (w/v) resulted in smooth, bead-free, and uniform nanofibers, which demonstrated improved molecular chain entanglement and stable jet dynamics. Further increasing the polymer concentration to 30% (w/v) produced homogeneous fibers with an elevated mean diameter of 411 ± 157 nm, confirming the enhanced jet stability and morphological integrity. Therefore, this concentration was selected as the optimal composition for the subsequent blending studies.

The surface morphologies of the electrospun HC/PVA nanofibers prepared from a 30% (w/v) total polymer solution at different blend ratios (70/30, 60/40, and 50/50 w/w) are presented in Fig. 4.

All samples exhibited continuous bead-free morphologies, confirming the stability and reproducibility of the needle-free electrospinning process. The mean fibre diameters

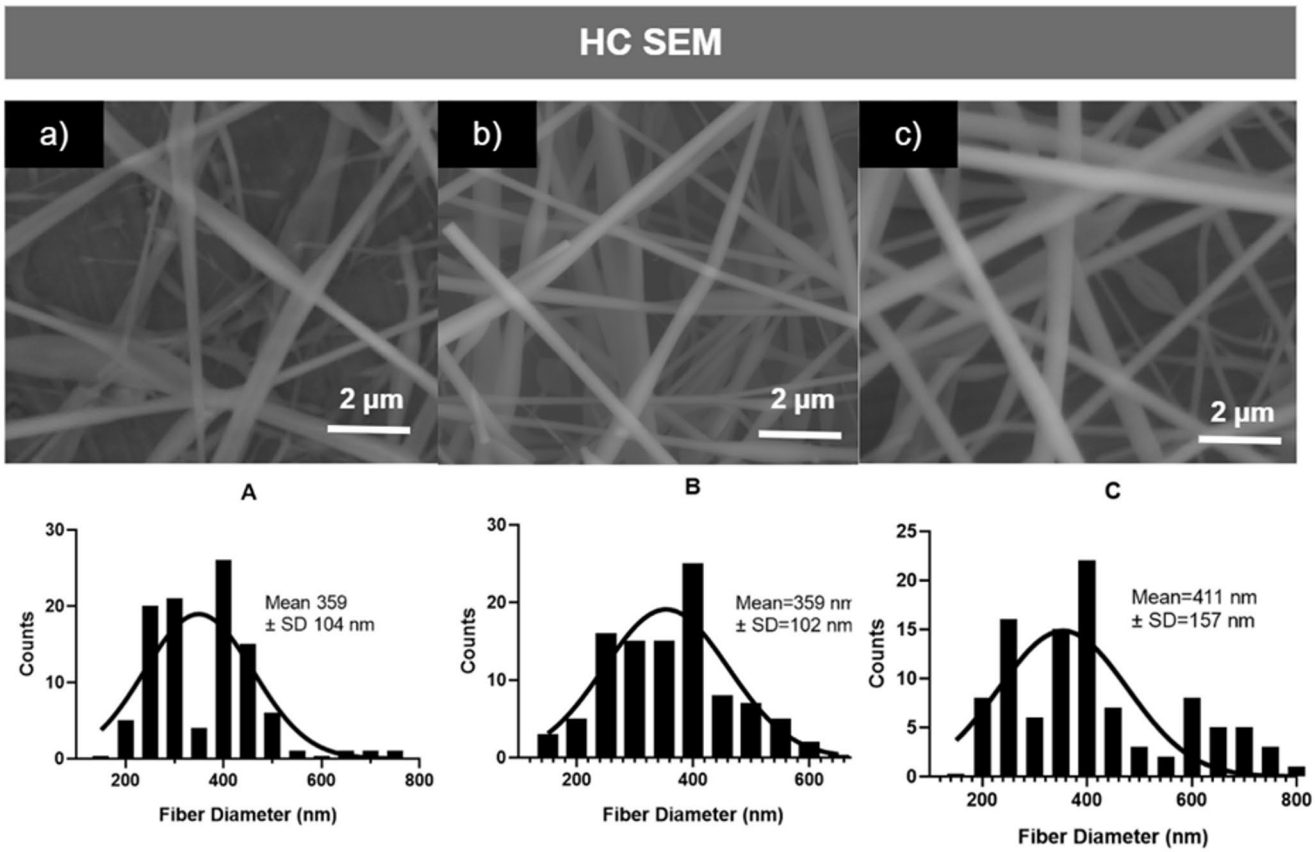


Fig. 3 SEM micrographs and corresponding fiber diameter distributions of electrospun HC nanofibers prepared with different polymer concentrations. (**a**) 20% w/v, (**b**) 25% w/v, and (**c**) 30% w/v

were 426 ± 53 nm for the 70/30 blend, 347 ± 70 nm for the 60/40 blend, and 316 ± 46 nm for the 50/50 blend. Increasing the HC fraction (70/30) increased the solution viscosity but reduced the electrical conductivity, resulting in thicker fibers owing to limited jet stretching. Conversely, increasing the PVA fraction improved charge transport and polymer chain flexibility, thereby facilitating greater jet elongation and the production of thinner and more uniform fibers. The 60/40 HC/PVA blend provided the best balance between viscoelastic stability and electrospinnability and was therefore selected for further functionalisation and biological evaluation.

The morphologies of the GA-crosslinked HC/PVA/CA nanofiber membranes (60/40, w/w) are shown in Fig. 5. All formulations containing CA extract (1–7% w/v, corresponding to 10% total triterpenes) exhibited smooth, bead-free, and continuous fibers, confirming the successful integration of CA and the stability of both the electrospinning and crosslinking processes. After exposure to 25% GA vapour at 25 ± 2 °C for 12 h, the nanofibers maintained their structural uniformity without swelling, fusion, or surface deformation. The mean fibre diameter slightly increased to 361 ± 80 nm, indicating moderate densification due to GA-induced interchain bonding, which restricted polymer chain mobility during jet stretching.

At low CA concentrations (1–3% w/v), the fibres displayed homogeneous diameters ranging from 367 ± 89 nm to 380 ± 79 nm. The hydrophilic triterpenoid compounds in CA enhanced the electrical conductivity and charge density of the spinning solution, resulting in more stable jet elongation and the formation of randomly oriented nanofibers with improved mechanical properties. However, further increasing the CA content (5–7% w/v) led to thicker fibers (404–451 nm), which was attributed to the enhanced intermolecular hydrogen bonding between the hydroxyl and carboxyl groups of CA triterpenes and the amide and hydroxyl groups of HC and PVA. These interactions increase the solution viscosity and restrict chain mobility, resulting in denser and more compact structures.

GA vapour crosslinking preserved the nanoscale uniformity and mechanical integrity of the CA-incorporated HC/PVA matrices, confirming the suitability of the selected parameters for producing stable, bioactive, and structurally cohesive nanofibrous scaffolds.

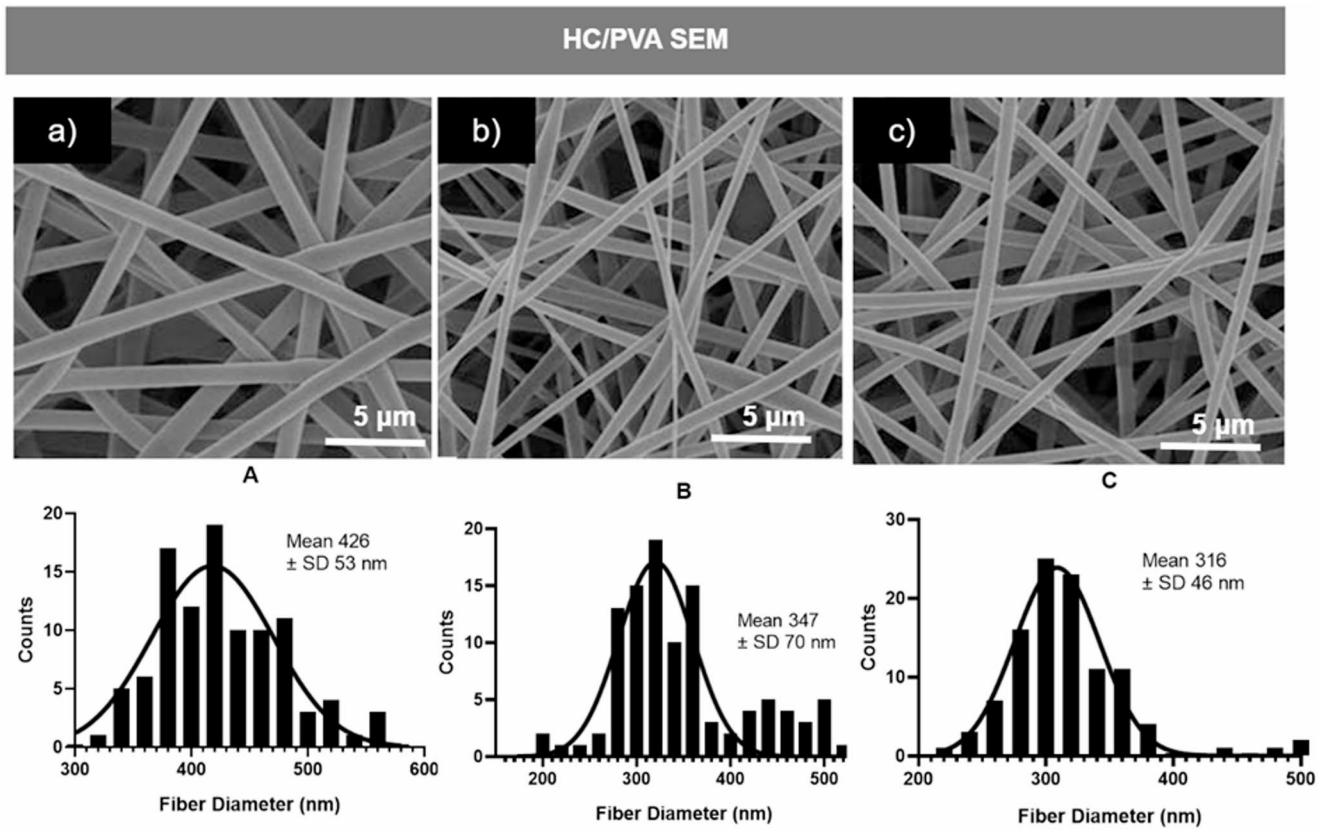


Fig. 4 SEM micrographs and fibre diameter distributions of HC/PVA nanofibers electrospun from a 30% (w/v) total polymer concentration at different blend ratios. (**a**) 70/30, (**b**) 60/40 and (**c**) 50/50

Fourier Transform Infrared (FTIR)

The chemical structures and intermolecular interactions of the electrospun nanofiber membranes were analysed using FTIR spectroscopy to confirm the successful blending of PVA and HC, incorporation of CA, and GA-induced crosslinking. The spectra of the individual components and the composite nanofibers are shown in Figs. 6 and 7, respectively.

The FTIR spectra of PVA, HC, the PVA/HC blend, and GA (Fig. 9) exhibited characteristic absorption bands of the constituent materials. PVA exhibited peaks at 3290 cm^{-1} (O–H stretching), 2930 cm^{-1} (C–H stretching), 1425 cm^{-1} (CH_2 bending), and 1090 cm^{-1} (C–O stretching). HC displayed a broad O–H/N–H stretching band (3300–3400 cm^{-1}), an amide I band at 1645 cm^{-1} (C=O stretching), and an amide II band at 1545 cm^{-1} (N–H bending and C–N stretching).

In the PVA/HC blend, partial overlapping and slight shifts of the hydroxyl and amide bands (O–H: 3275 cm^{-1}; amide I: 1638 cm^{-1}) confirmed hydrogen bonding between PVA hydroxyl and HC amide/carboxyl groups. These interactions reduced segmental chain mobility and promoted a denser and more uniform fibrous morphology, consistent with the SEM observations. After GA vapor crosslinking, a new band appeared at 1720 cm^{-1}, accompanied by a shift of the amide I band to 1635 cm^{-1}, indicating imine (C=N) linkage formation between the GA aldehyde and polymer aminohydroxyl groups. The decreased O–H intensity reflected partial hydroxyl consumption through acetalisation, confirming successful crosslinking and enhanced structural rigidity within the polymer network.

The FTIR spectra of the pure CA and CA-loaded PVA/HC/GA nanofibers containing 1–7% (w/v) CA are shown in Fig. 10. Pure CA exhibited characteristic peaks at 3410 cm^{-1} (O–H stretching), 2930 cm^{-1} (C–H stretching), 1715 cm^{-1} (C=O stretching), 1610 cm^{-1} (C=C stretching), and 1075 cm^{-1} (C–O–C stretching). In the CA-loaded nanofibers, these peaks shifted toward lower wavenumbers and decreased in intensity, confirming the formation of hydrogen bonds between CA triterpenes and the polymer matrix. The broadening of the O–H band (3200–3400 cm^{-1}) with increasing CA content indicates multiple hydrogen bridges between the CA hydroxyl/carboxyl and HC/PVA functional groups.

After GA crosslinking, the 1715 cm^{-1} carbonyl band decreased, and weak shoulders appeared at 1650–1630 cm^{-1}, indicating aldehyde consumption and C=N bond formation. These molecular rearrangements confirm the coexistence of

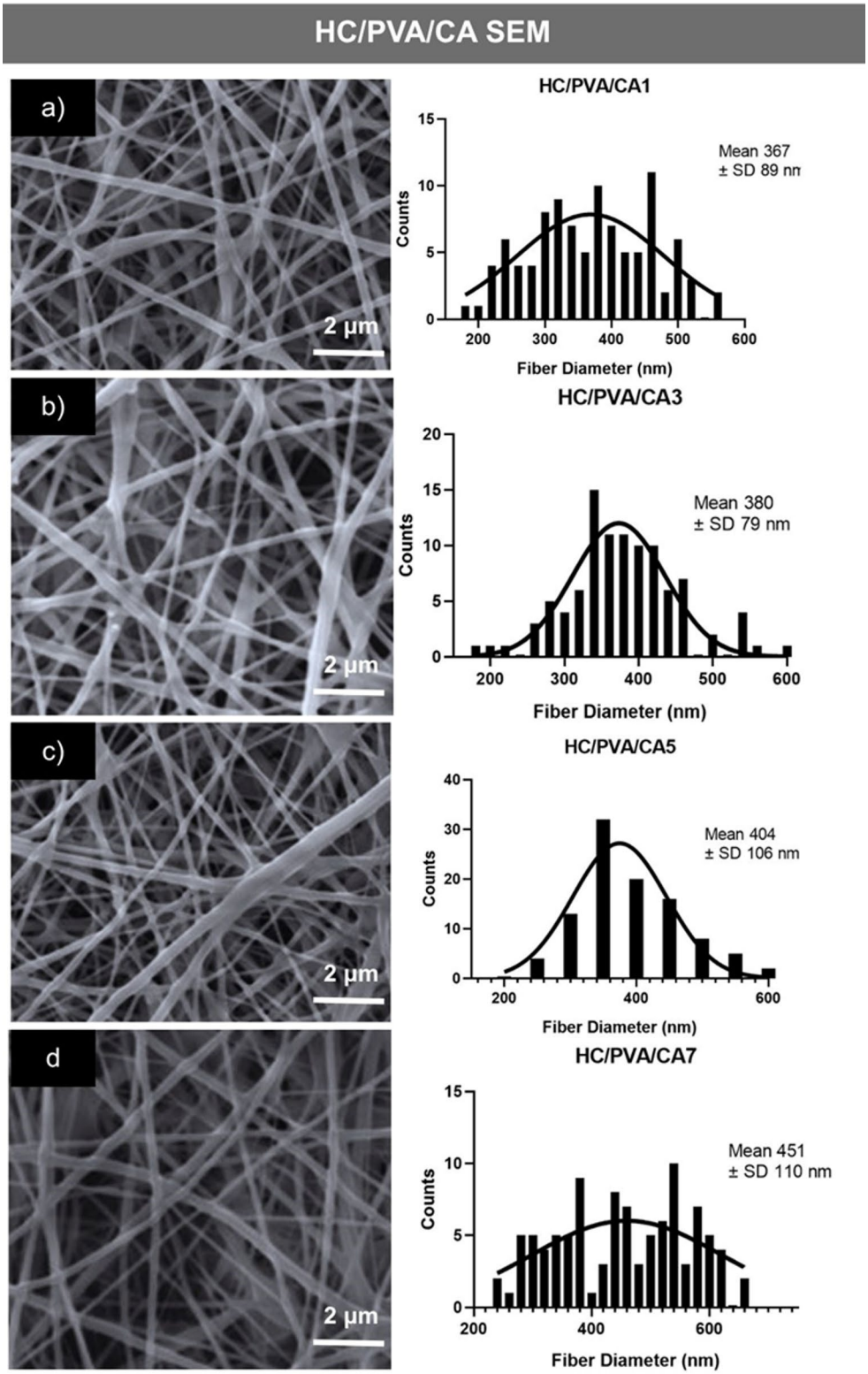


Fig. 5 Fiber diameter distributions of HC/PVA nanofibers containing increasing concentrations of CA extract (1–7% w/v and 10% total triterpenes)

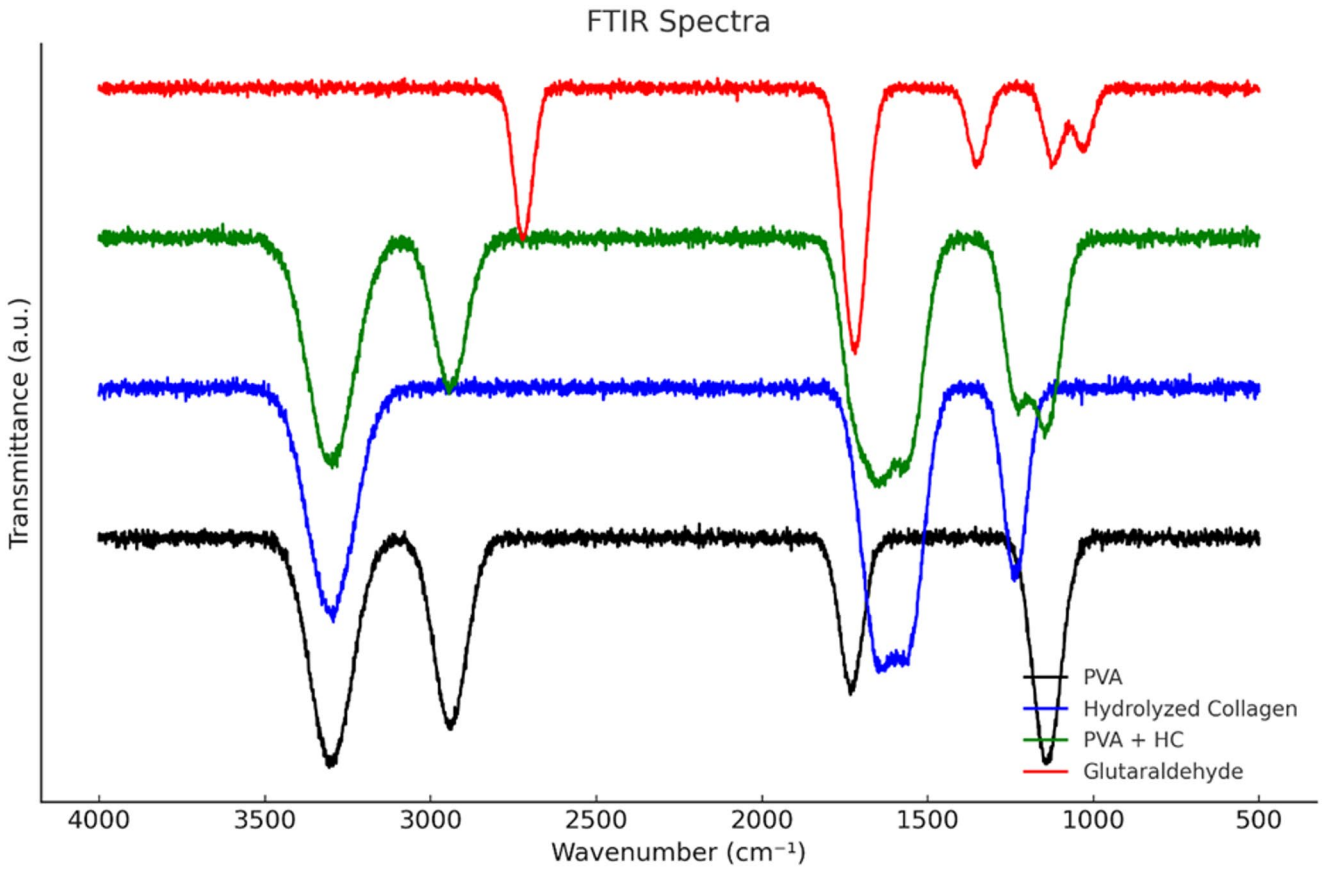


Fig. 6 FTIR spectra of PVA, HC, PVA/HC blend, and GA, showing the characteristic functional groups of GA-induced crosslinking

physical (hydrogen-bonded) and chemical (GA-mediated) crosslinking within the nanofibrous matrix. This dual mechanism enhanced molecular packing, reduced free volume, and contributed to increased fiber diameter and morphological uniformity in CA-enriched samples.

Rheological Analysis

Table 1 presents the rheological characterization results. The addition of CA increased the viscosity from 485 ± 12 cP (control) to 742 ± 18 cP (7% CA), which was attributed to enhanced hydrogen bonding and chain entanglements from triterpenoid hydroxyl groups. The electrical conductivity increased systematically (from 1250 to 1720 µS/cm), which facilitated jet formation during electrospinning. The surface tension decreased (from 42.3 to 34.5 mN/m), improving the spreadability of the solution.

Mechanical Analysis

Table 2 presents the mechanical characterization of the pure-component and composite nanofiber membranes. Pure HC nanofibers demonstrated relatively low tensile strength (1.42 ± 0.18 MPa) and Young's modulus (45.3 ± 6.2 MPa) owing to the weak intermolecular forces in the hydrolyzed protein structure. Pure PVA exhibited superior mechanical properties, with a tensile strength of 5.28 ± 0.42 MPa and Young's modulus of 185.6 ± 15.8 MPa, which is characteristic of its semicrystalline polymeric nature and strong hydrogen bonding network. Pure CA extract formed brittle films unsuitable for mechanical testing, indicating its role as a bioactive additive rather than as a structural component. Pure CA extract could not be electrospun into coherent nanofiber membranes because of its insufficient molecular weight and chain entanglement, which prevented the formation of mechanically testable specimens. The blended HC/PVA control formulation achieved intermediate mechanical performance (3.85 ± 0.28 MPa tensile strength and 118.2 ± 10.5 MPa modulus), demonstrating synergistic polymer chain interactions. The incorporation of CA into the HC/PVA matrix induced concentration-dependent mechanical modulation. At 3% CA loading, the nanofibers achieved maximum tensile strength (4.82 ± 0.34 MPa) and Young's modulus (142.5 ± 12.3 MPa), representing 25.2% and 20.6% enhancements relative to the control, respectively. This mechanical reinforcement mechanism involves hydrogen bonding interactions between hydroxyl-rich triterpene structures (asiaticoside and madecassoside) and

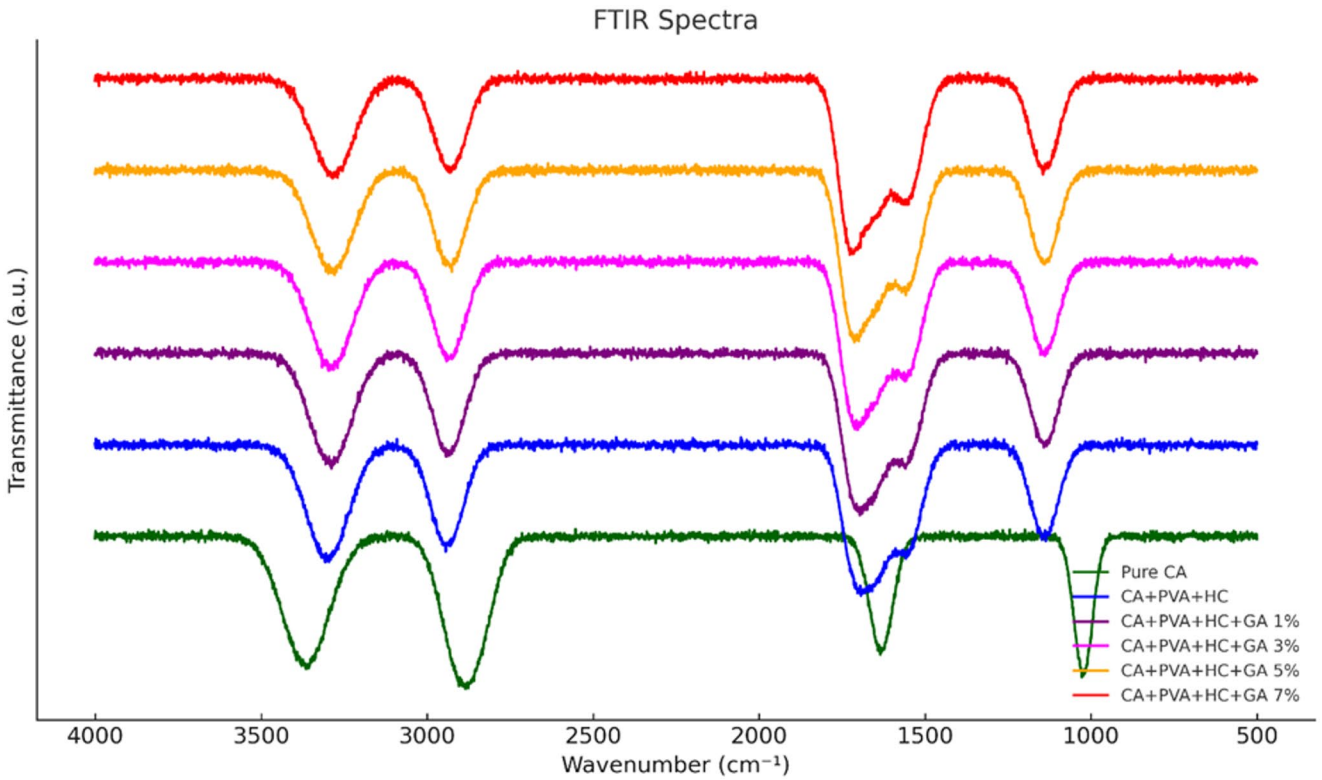


Fig. 7 FTIR spectra of CA and CA-loaded PVA/HC/GA nanofiber membranes with different CA concentrations (1–7% w/v) between CA and polymeric matrix

Table 1 Rheological properties of HC/PVA/CA solutions at different CA concentrations (mean ± SD, $n = 3$)

Sample	Viscosity (cP)	Conductivity (μS/cm)	Surface Tension (mN/m)
Pure HC	125 ± 8	890 ± 25	48.5 ± 1.5
Pure PVA	285 ± 10	620 ± 18	44.2 ± 1.3
Pure CA	45 ± 5	1850 ± 55	32.8 ± 1.8
HC/PVA	485 ± 12	1250 ± 35	42.3 ± 1.2
HC/PVA/CA 1%	528 ± 15	1310 ± 28	40.8 ± 0.9
HC/PVA/CA 3%	582 ± 18	1425 ± 42	38.5 ± 1.1
HC/PVA/CA 5%	658 ± 22	1580 ± 38	36.2 ± 1.3
HC/PVA/CA 7%	742 ± 18	1720 ± 45	34.5 ± 1.0

Table 2 Mechanical properties of HC/PVA/CA nanofibers (mean ± SD, $n = 5$)

Sample	Tensile Strength (MPa)	Young's Modulus (MPa)	Elongation at Break (%)
Pure HC	1.42 ± 0.18	45.3 ± 6.2	15.8 ± 2.4
Pure PVA	5.28 ± 0.42	185.6 ± 15.8	52.3 ± 4.6
HC/PVA	3.85 ± 0.28	118.2 ± 10.5	42.8 ± 3.5
HC/PVA/CA 1%	4.12 ± 0.31	128.5 ± 11.2	40.5 ± 3.1
HC/PVA/CA 3%	4.82 ± 0.34	142.5 ± 12.3	38.5 ± 3.2
HC/PVA/CA 5%	4.15 ± 0.29	125.8 ± 9.8	35.2 ± 2.8
HC/PVA/CA 7%	3.58 ± 0.26	108.5 ± 8.5	31.8 ± 2.5

polymer chains, promoting enhanced molecular entanglement and effective stress transfer throughout the nanofiber network.

Higher CA concentrations (5% and 7%) exhibited reduced mechanical properties compared to the 3% formulation, with tensile strengths of 4.15 ± 0.31 MPa and 3.62 ± 0.29 MPa, respectively. This decline is attributed to the disruption of HC-PVA intermolecular interactions and potential plasticizing effects at excessive CA loading, where triterpene molecules interfere with optimal polymer chain packing rather than reinforcing it. The 3% CA formulation maintained adequate elongation at break (38.5 ± 3.2%), demonstrating sufficient flexibility and conformability required for wound dressing applications to accommodate irregular wound geometries and patient movement without mechanical failure.

Water Retention

Figure 8 presents the equilibrium water retention behavior of GA-crosslinked HC/PVA (60/40, w/w) and CA-loaded nanofiber membranes after 48 h immersion in distilled water. The pristine HC/PVA membrane exhibited the lowest water retention capacity among all formulations. Although both HC and PVA possess abundant hydroxyl groups, GA vapor crosslinking restricts polymer chain mobility and reduces

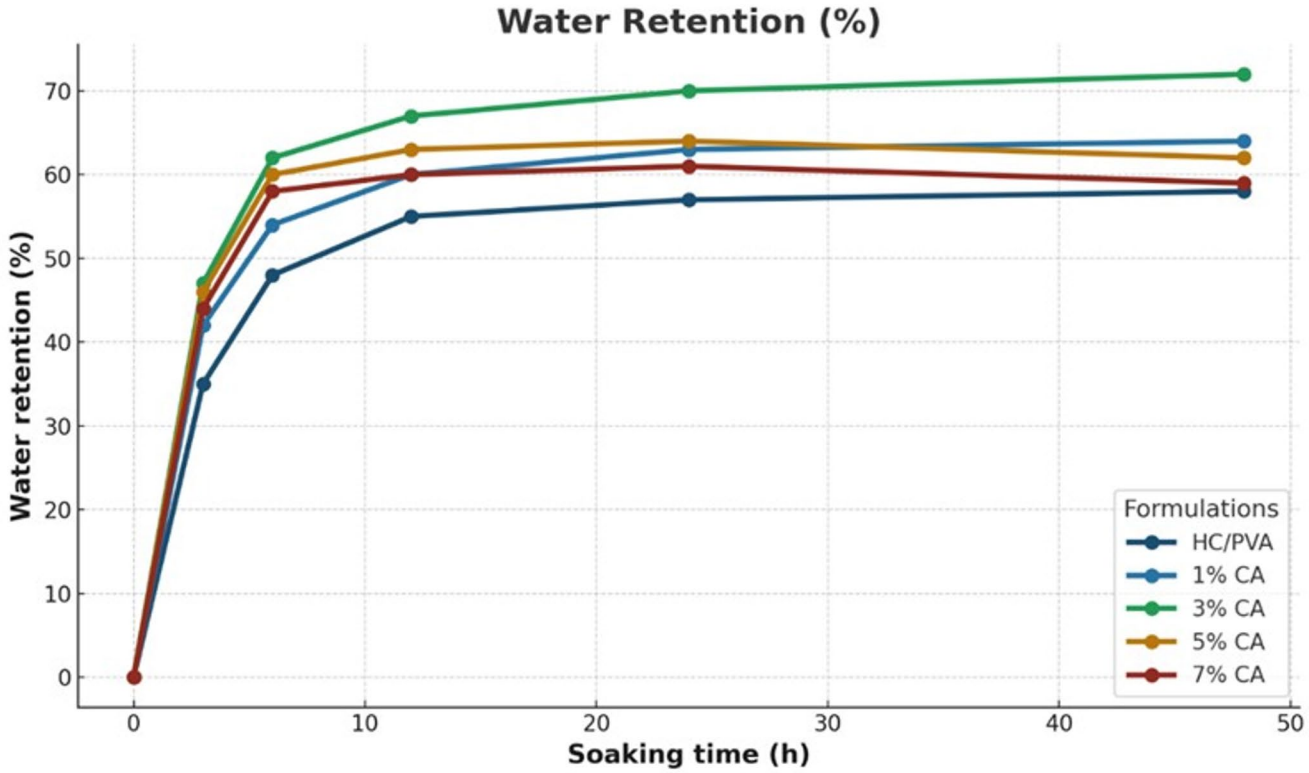


Fig. 8 Water retention behavior of HC/PVA and CA-enriched nanofiber membranes after 48 h immersion in distilled water

Table 3 Water retention (%) of HC/PVA/CA nanofibers at different pH values

pH	HC/PVA (%)	1% CA (%)	3% CA (%)	5% CA (%)	7% CA (%)
5.4	220	260	320	300	280
7.4	180	210	260	240	220
9.0	130	150	190	180	160

the free volume available for water diffusion, thereby limiting the swelling capacity of the neat membrane.

Table 3 summarizes the equilibrium water retention values obtained at pH 5.4, 7.4, and 9.0. These pH conditions were selected to simulate physiologically relevant environments. pH 7.4 (PBS) represents normal physiological conditions, pH 5.4 mimics the mildly acidic microenvironment observed in chronic or infected wounds, and pH 9.0 was used as an alkaline stress condition to evaluate structural stability under extreme conditions.

The incorporation of CA significantly enhanced the water retention capacity of the membranes at all tested pH values. The 3% CA formulation exhibited the highest water uptake, reaching 320% at pH 5.4 and 260% at pH 7.4. This behavior indicates an optimal balance between hydrophilic functional groups and structural porosity. The hydroxyl (–OH) and carboxyl (–COOH) groups present in CA contribute to additional hydrogen bonding interactions with water molecules, thereby increasing hydration capacity without excessively restricting network expansion.

At higher CA loadings (5–7%), a moderate decrease in water retention was observed. This reduction may be attributed to intensified intermolecular interactions within the polymer matrix, leading to partial densification of the fibrous network and reduced effective pore accessibility. Excessive hydrogen bonding between CA and HC/PVA chains can limit chain relaxation and restrict water diffusion pathways.

Water retention was consistently higher under acidic conditions (pH 5.4) compared to neutral and alkaline environments. This trend can be associated with protonation effects and reduced electrostatic repulsion within the polymer network, facilitating enhanced water accommodation. Conversely, the alkaline condition (pH 9.0) resulted in lower swelling values, likely due to increased chain rigidity and reduced hydrogen bonding efficiency.

Importantly, all membranes maintained their structural integrity throughout the 48 h immersion period, confirming that GA vapor-phase crosslinking (25%, 25 °C, 12 h) provided sufficient stabilization while preserving hydrophilic functionality.

Weight Loss

Figure 9 illustrates the hydrolytic degradation behavior of GA-crosslinked HC/PVA (60/40, w/w) and CA-loaded nanofiber membranes during immersion in distilled water and PBS (pH 7.4) at 37 °C for 21 days. All formulations exhibited progressive weight loss over time, confirming gradual hydrolytic disintegration of the polymeric network.

The pristine HC/PVA membrane showed the highest degradation, reaching 68.8% weight loss in distilled water and 42.5% in PBS at day 21. The greater mass loss observed in distilled water compared to PBS (approximately 62%

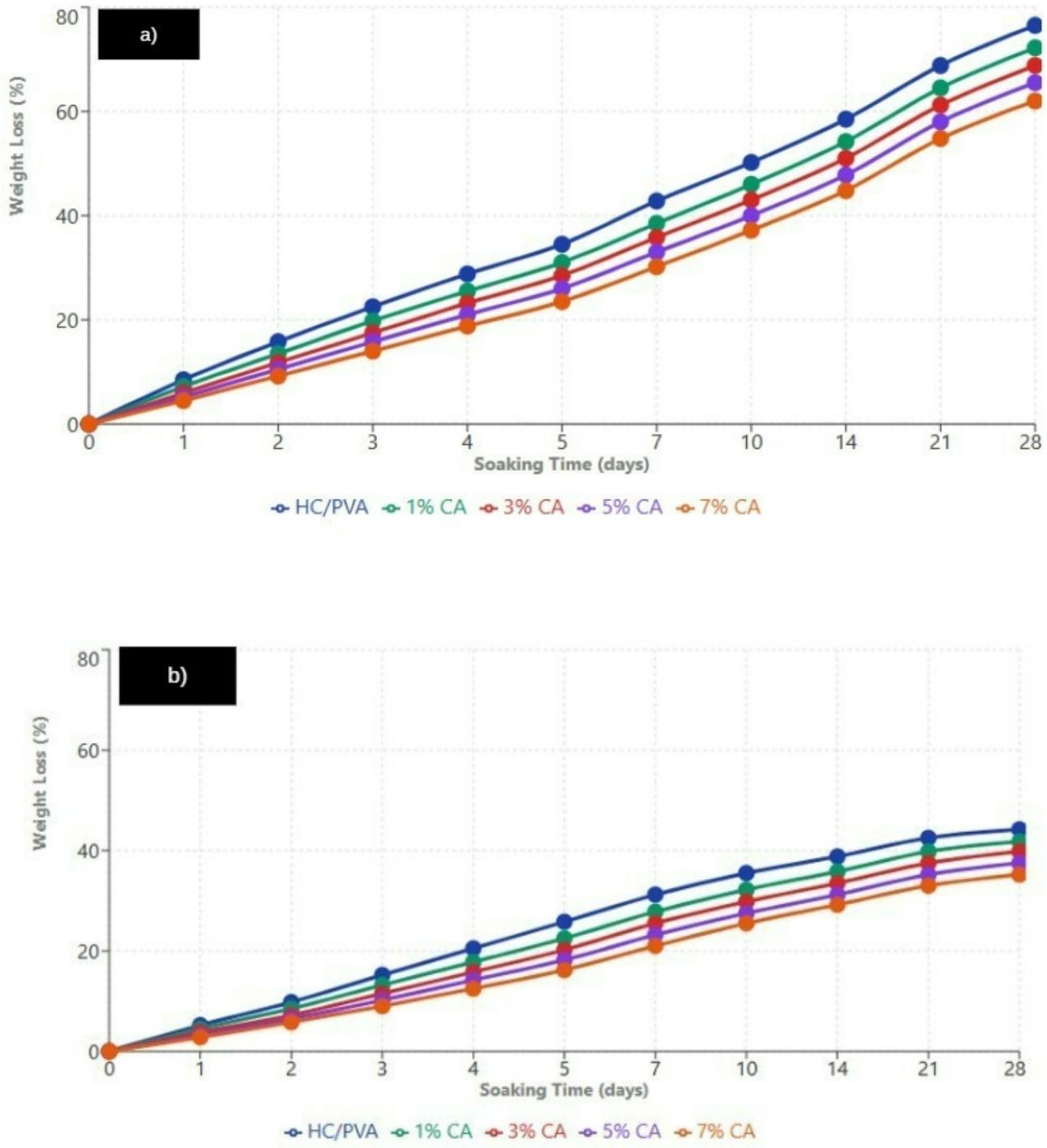


Fig. 9 Biodegradation behavior of HC/PVA and CA-enriched nanofiber membranes during immersion in (a) distilled water and (b) PBS (pH 7.4) at 37 °C for 21 days. Data are presented as mean ± SD ($n = 3$)

higher relative to PBS at day 21) can be attributed to enhanced water penetration and swelling in the absence of ionic strength, which promotes polymer chain relaxation and dissolution.

The incorporation of CA reduced the overall degradation in a concentration-dependent manner. The 7% CA formulation exhibited the lowest weight loss, with 54.8% in distilled water and 33.0% in PBS at day 21, corresponding to an approximately 20% reduction in mass loss compared to the pristine membrane. This stabilizing effect is likely associated with additional intermolecular hydrogen bonding interactions between CA triterpenoids and the HC/PVA matrix, which reinforce the polymer network and restrict chain mobility.

Among the tested formulations, the 3% CA membrane exhibited a balanced degradation profile, showing 39.8% weight loss in PBS at day 21. Such controlled degradation behavior may be advantageous for wound dressing applications requiring gradual material resorption over a clinically relevant timeframe.

1.1 Cell Analysis

3.2.1. Cytotoxicity and proliferation

The cytotoxic potential, cell proliferation (142.3 ± 8.5% viability on day 7), and collagen synthesis (238.5 ± 15.2% relative to control) of the HC/PVA/CA nanofiber membranes were investigated using NIH-3T3 fibroblasts after 48 h of incubation, as shown in Fig. 10.

The MTT assay revealed an apparent dose-dependent effect of Centella asiatica (CA) on fibroblast proliferation. Incorporation of CA at 1% and 3% resulted in a pronounced enhancement of cell proliferation compared to the control, with 3% CA showing the highest cell number in the series. This increase can be attributed to the bioactive triterpenoids (Asiaticoside and Madecassoside) in CA extract, which are known to stimulate fibroblast migration, collagen synthesis, and mitotic activity. Statistical analysis confirmed that these enhancements were significant ($p < 0.05$), verifying that moderate CA concentrations promote fibroblast viability and proliferation without inducing cytotoxicity.

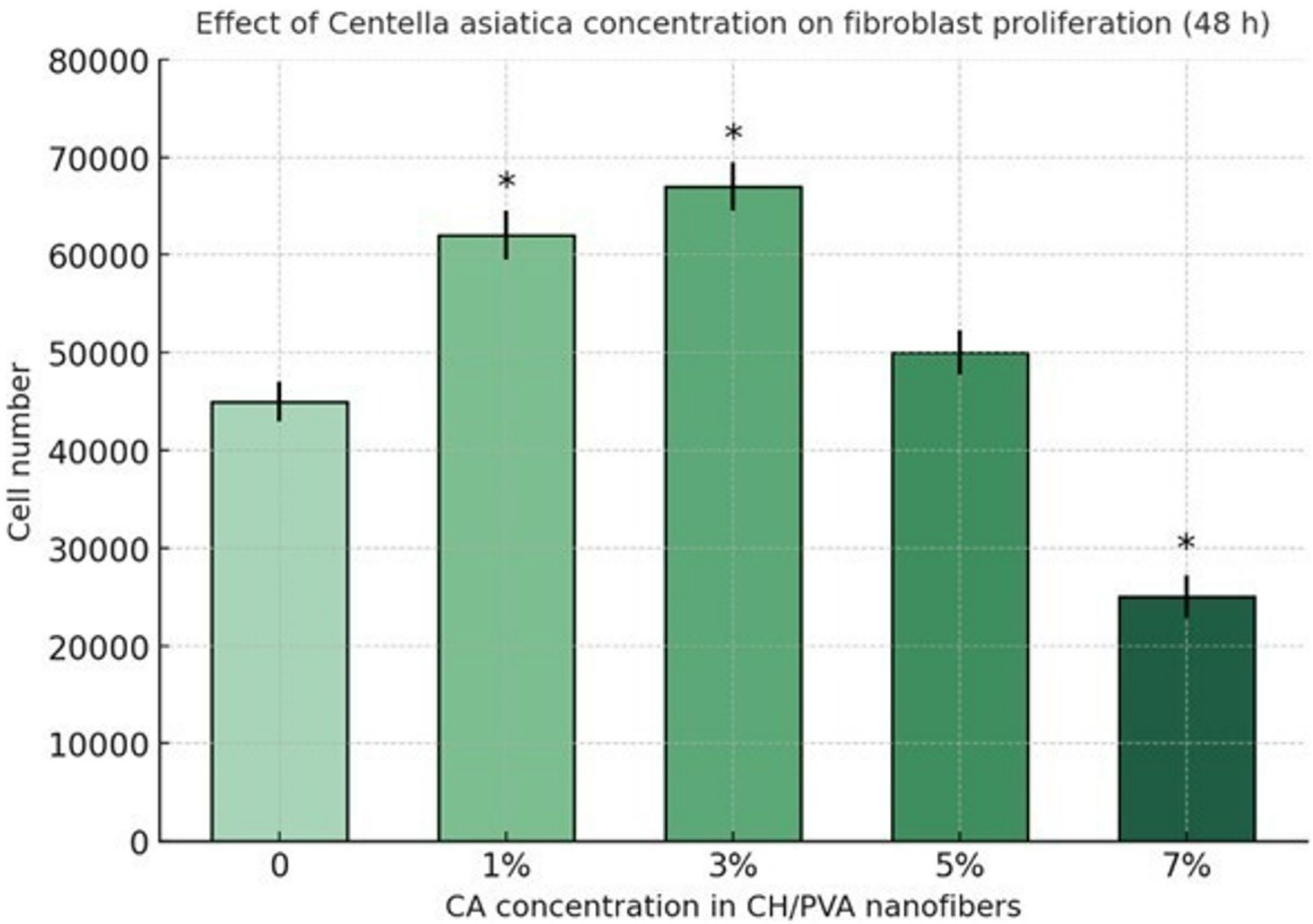


Fig. 10 Effect of Centella asiatica concentration (0–7%) on fibroblast proliferation after 48 h of incubation. The highest proliferation was observed with 3% CA, whereas cell viability decreased with higher extract concentrations. Statistical significance was determined using one-way ANOVA with Tukey's post-hoc test

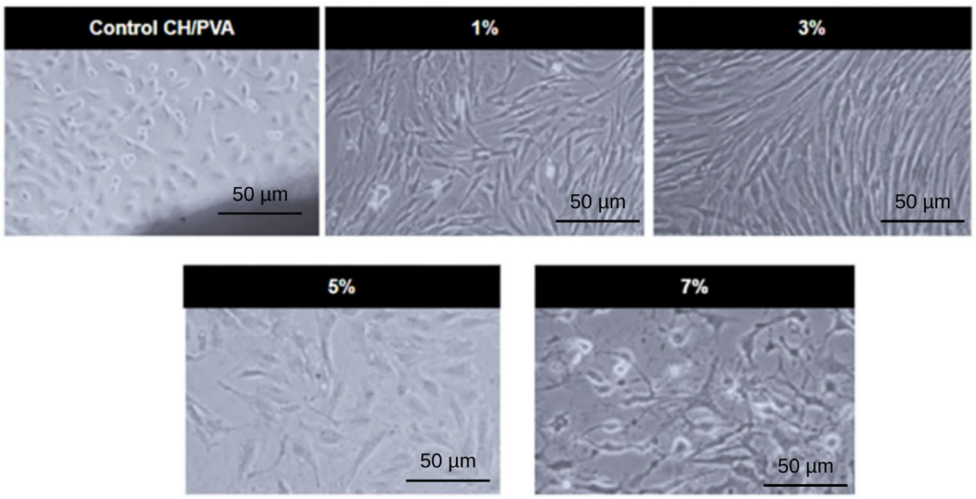


Fig. 11 Light microscopy images of NIH-3T3 fibroblasts cultured on HC/PVA/CA nanofiber membranes with various CA concentrations (0, 1, 3, 5, and 7%). Fig. Cells on 1% and 3% CA membranes displayed elongated and confluent morphologies, whereas higher CA loadings resulted in reduced adhesion and rounded cell shapes, indicating decreased viability

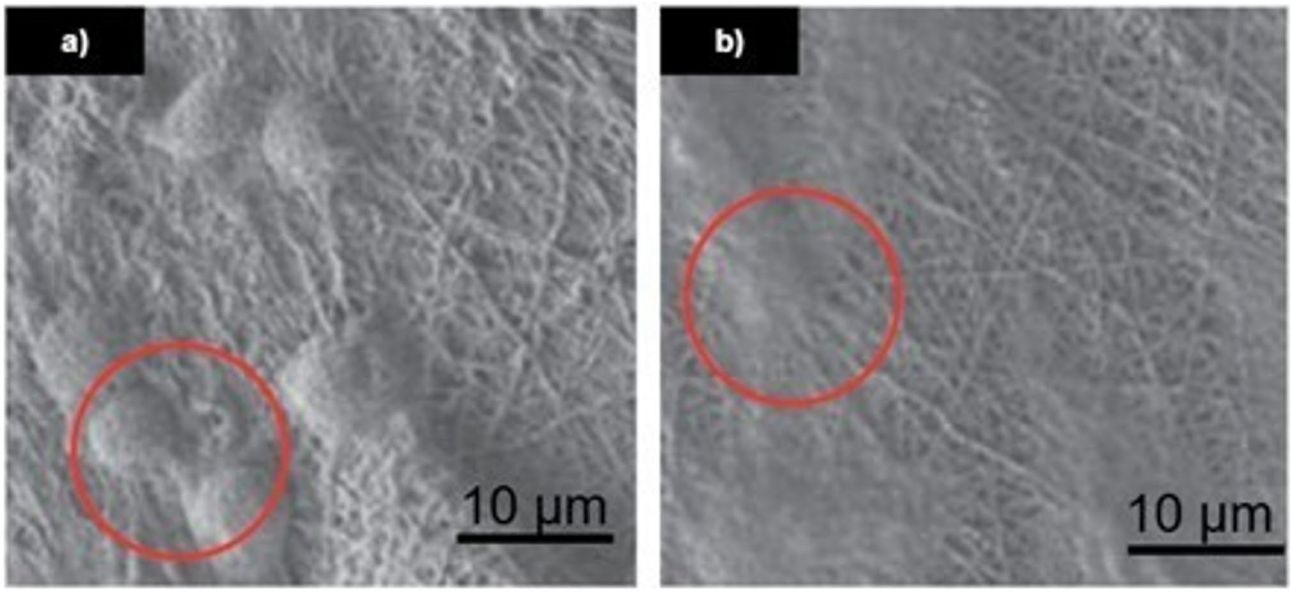


Fig. 12 Scanning electron micrographs showing the fibroblast morphology on (a) HC/PVA and (b) HC/PVA/CA nanofiber membranes after 48 h of incubation. Circles indicate cells. Cells on the HC/PVA/CA scaffolds exhibited extensive filopodia and interconnected spreading across the fibres, whereas cells on the pure HC/PVA scaffolds showed limited adhesion and fewer anchorage points

An increase in CA concentration above 5% resulted in a corresponding decrease in cell number, with the lowest viability observed at 7% CA. This decline may be attributed to the excessive presence of phenolic and triterpenoid constituents, which can slightly alter local pH and oxidative balance, leading to mild cytotoxic stress.

Light microscopy observations (Fig. 11) were consistent with the results of the MTT assay. Fibroblast cells cultured on 1% and 3% CA nanofiber membranes exhibited an elongated spindle-shaped morphology and dense confluence, indicative of healthy adhesion, spreading, and proliferation. In contrast, cells grown on 5% CA membranes showed partial detachment and reduced density, whereas those grown on 7% CA membranes appeared rounded and shrunken, indicating a decrease in cell viability.

As shown in Fig. 12(a), fibroblasts cultured on HC/PVA (60/40, w/w) membranes exhibited moderate adhesion with limited spreading and maintained a flattened spindle-shaped morphology. The relatively smooth and compact fiber surface restricted extensive anchorage formation, indicating that, although the base matrix was nontoxic, its surface chemistry alone provided suboptimal cues for cellular proliferation (142.3 ± 8.5% viability on day 7), collagen synthesis (238.5 ± 15.2% relative to the control), and spreading.

Figure 12(b) illustrates the attachment of fibroblasts to the HC/PVA/CA nanofibers containing Centella asiatica extract (10% total triterpenes). The cells displayed abundant

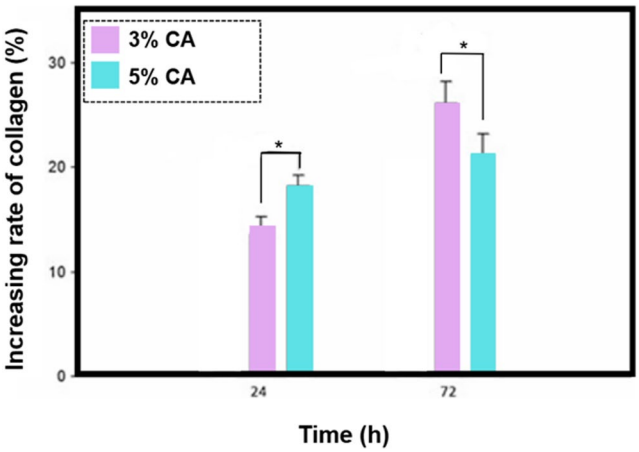


Fig. 13 Collagen synthesis rates of NIH-3T3 fibroblasts cultured on HC/PVA/CA nanofiber membranes containing 3% and 5% CA extract after 24 and 72 h. Both CA-containing membranes showed significantly enhanced collagen secretion compared with the control group ($n=3$; $p<0.05$). Statistical analysis was performed using one-way ANOVA, followed by Tukey's post-hoc test

filopodial extensions and firm contact with adjacent fibres, forming a continuous cellular network throughout the scaffold. This enhanced cell–substrate interaction is attributed to the bioactive triterpenoid constituents of CA, mainly asiaticoside and madecassoside, which have been reported to stimulate fibroblast migration, extracellular matrix deposition, and collagen biosynthesis.

Furthermore, the incorporation of CA increased the surface hydrophilicity and roughness of the nanofibers, thereby promoting serum protein adsorption and integrin-mediated adhesion. These physicochemical and biochemical modifications collectively facilitated improved fibroblast attachment, spreading, and communication across the fibrous architecture, thereby confirming the favourable bioactivity of the CA-modified nanofibrous matrix.

3.2.2. Collagen synthesis activity of fibroblasts

The collagen synthesis activity of NIH-3T3 fibroblasts cultured on HC/PVA/CA nanofiber membranes was investigated after 24 and 72 h of incubation to evaluate the influence of CA incorporation on extracellular matrix (ECM) formation. The quantitative results are shown in Fig. 13.

After 24 h of culture, fibroblasts on the 3% CA membrane exhibited an approximately 16% increase in collagen synthesis compared to the control, while those on the 5% CA membrane showed a slightly higher increase of approximately 18%. This initial enhancement suggests that the triterpenoid compounds in CA (such as Asiaticoside and Madecassoside) provide biochemical stimuli that promote fibroblast metabolic activity and early collagen secretion.

Table 4 Inhibition zone diameters of HC/PVA/CA nanofibers against *S. aureus* and *E.* coli (mean ± SD, $n=3$)

Sample	S. aureus (mm)	E. coli (mm)
HC/PVA	7.2 ± 0.8	6.8 ± 0.7
HC/PVA/CA 1%	9.5 ± 0.8	8.5 ± 0.7
HC/PVA/CA 3%	11.5 ± 0.9*	10.2 ± 0.8*
HC/PVA/CA 5%	14.2 ± 1.1**	12.8 ± 0.9**
HC/PVA/CA 7%	12.8 ± 1.0*	11.5 ± 0.8*
Gentamicin (10 µg)	22.5 ± 1.5	20.8 ± 1.3

*$p<0.05$, **$p<0.01$ vs. HC/PVA control

At 72 h, the collagen synthesis rate further increased in both groups; however, fibroblasts on the 3% CA membrane demonstrated the highest collagen accumulation (approximately 30% higher than that of the control), whereas the 5% CA membrane maintained an increase of approximately 25%. Although both formulations significantly promoted collagen synthesis ($p<0.05$), the difference between the 3% and 5% CA groups was not statistically significant at 72 h. This indicates that higher CA concentrations do not proportionally enhance ECM biosynthesis.

The slight decrease observed with 5% CA may be related to the excessive presence of phenolic and triterpenoid compounds, which can alter the oxidative equilibrium of the local microenvironment and impose mild cytotoxic stress on fibroblasts. Consequently, while the incorporation of CA at moderate levels enhances cell metabolism and matrix synthesis, excessive loading may reduce cellular activity owing to biochemical saturation effects.

The enhanced fibroblast activity at 1–3% CA was attributed to optimal bioactive triterpenes that stimulated TGF-β signalling pathways, promoting cell adhesion and collagen synthesis (238.5 ± 15.2% at 3% CA). At this range, nanofibers provide ideal surface properties and mechanical characteristics (4.82 ± 0.34 MPa tensile strength) that mimic the native ECM. Higher CA concentrations (5–7%) exceed the cytotoxicity threshold, causing membrane disruption and metabolic interference, thereby reducing cell viability.

Antibacterial Assay

The antibacterial activities of the HC/PVA/CA nanofiber membranes against S. aureus and E. coli were evaluated using the disc diffusion method. The mean diameters of the inhibition zones are presented in Table 4, and the corresponding agar diffusion images are shown in Fig. 14. Based on the results, the HC/PVA/CA nanofibers demonstrated **bacteriostatic activity** against *S. aureus* and *E. coli*. The moderate inhibition zones (14.2 ± 1.1 mm and 12.8 ± 0.9 mm, respectively) and concentration-dependent response suggest that the membranes inhibit bacterial growth rather than cause direct cell death. This bacteriostatic mechanism is attributed to the triterpene-rich CA extract, which disrupts bacterial

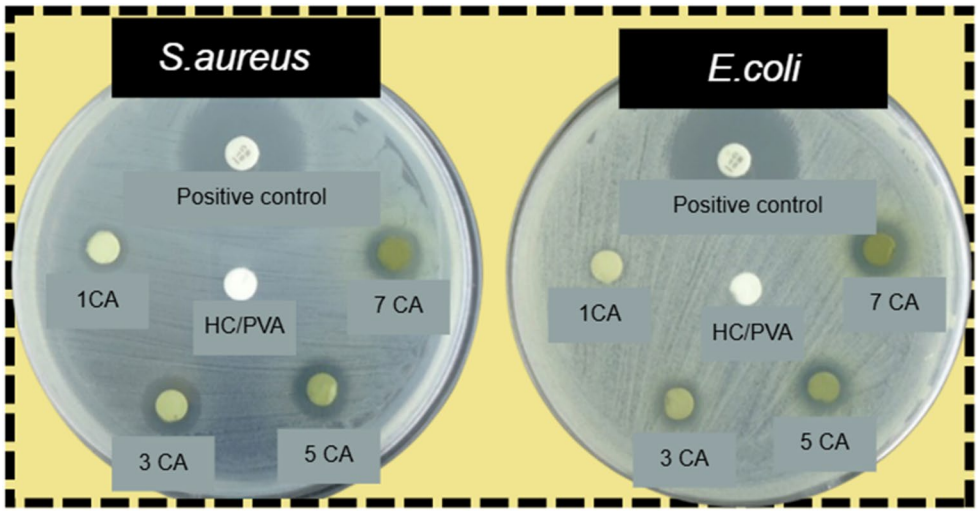


Fig. 14 Antibacterial activity of crosslinked HC/PVA and crosslinked HC/PVA/CA nanofiber membranes against *S. aureus* (*Gram-positive*) and *E. coli* (*Gram-negative*) determined by the agar diffusion plate test

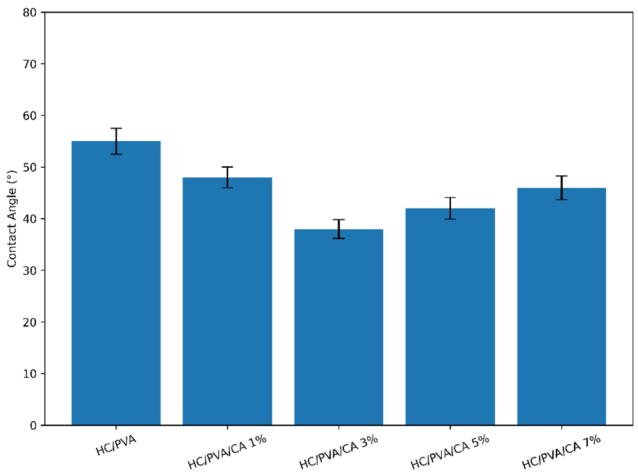


Fig. 15 Contact angle measurements of GA-crosslinked HC/PVA and HC/PVA/CA nanofiber membranes. Data are presented as mean ± standard deviation (SD) ($n = 3$)

metabolism and membrane functions. For wound dressing applications, bacteriostatic activity offers advantages, including sustained infection control and reduced inflammatory responses compared to bactericidal agents.

The control HC/PVA-crosslinked membranes showed no inhibition zones against *S. aureus* or *E. coli*, confirming the absence of intrinsic antibacterial functionality in the polymeric matrix. The average diameters of the inhibition zones of the HC/PVA/CA nanofibers against *S. aureus and E. coli* are presented in Table 4.

The incorporation of CA resulted in distinct inhibition halos, particularly in formulations containing 3% and 5% CA, which exhibited the most substantial inhibition zones of approximately 13–14 mm for *S. aureus* and 12–13 mm for *E. coli*. This pronounced antibacterial response is attributed to the bioactive triterpenoids (Asiatic acid, madecassic acid, and asiaticoside) and phenolic constituents present in CA.

A slight reduction in the inhibition zone was observed at 7% CA, suggesting limited diffusion of bioactive compounds from the nanofiber matrix. Higher CA loadings have been shown to increase the matrix density and reduce solubility, which may explain the observed effect. Despite this minor decrease, all CA-incorporated membranes displayed significant antibacterial activity relative to the control, confirming that Centella asiatica effectively imparts antimicrobial properties to the HC/PVA nanofibrous wound-dressing system.

Wettability (Contact Angel)

The contact angle measurements presented in Fig. 15 demonstrate a clear composition-dependent variation in surface wettability among the GA-crosslinked nanofiber membranes. The pristine HC/PVA (60/40, w/w) membrane exhibited a contact angle of 55.0 ± 2.5°, indicating moderate hydrophilicity. Upon incorporation of CA, the contact angle progressively decreased to 48.0 ± 2.0° (1% CA) and reached the lowest value at 3% CA (38.0 ± 1.8°), confirming enhanced surface polarity and improved water spreading. At higher CA loadings (5–7%), a slight increase in contact angle was observed, suggesting partial surface densification due to intensified intermolecular interactions. Overall, the 3% CA formulation exhibited the most favorable wettability profile.

Conclusions

This study successfully developed environmentally responsible HC/PVA/CA nanofiber membranes via fully water-based needleless electrospinning for advanced wound-healing applications. The exclusive use of distilled water as solvent eliminated toxic organic solvents such

as DMF and chloroform, thereby substantially reducing solvent-related environmental burden and occupational exposure risks commonly associated with conventional electrospinning processes.

Systematic optimisation of CA incorporation (1–7% w/v) demonstrated that the 3% CA formulation achieved the most balanced physicochemical, mechanical, and biological performance. This composition exhibited superior mechanical characteristics, with a tensile strength of 4.82 ± 0.34 MPa and a Young's modulus of 142.5 ± 12.3 MPa, representing a 25.2% and 20.6% improvement, respectively, over the HC/PVA control matrix. Rheological evaluation confirmed that 3% CA increased viscosity (582 ± 18 cP) and conductivity (1425 ± 42 µS/cm) to levels optimal for stable jet formation and uniform bead-free nanofibers. Furthermore, the 3% CA membranes exhibited the most favourable wettability profile (38.0 ± 1.8° contact angle) and the highest water retention capacity under physiologically relevant conditions (260% at pH 7.4; 320% at pH 5.4), indicating an optimal balance between hydrophilicity and structural integrity.

Biologically, HC/PVA/CA (3%) nanofibers significantly enhanced NIH-3T3 fibroblast viability (142.3 ± 8.5%) and collagen synthesis (238.5 ± 15.2% relative to control, $p < 0.05$), confirming the stimulatory role of triterpenoid compounds in extracellular matrix regeneration. SEM observations revealed improved cell spreading and extensive filopodia formation on CA-modified scaffolds, supporting enhanced integrin-mediated adhesion. Antibacterial assessment demonstrated concentration-dependent bacteriostatic activity, with the largest inhibition zones observed at 5% CA against *Staphylococcus aureus* (14.2 ± 1.1 mm) and *Escherichia coli* (12.8 ± 0.9 mm). Notably, 3% CA provided the most effective balance between cytocompatibility and antimicrobial performance, highlighting the importance of dosage optimisation.

From a sustainability perspective, although glutaraldehyde (GA) is inherently a reactive aldehyde compound, its application via vapor-phase crosslinking in a sealed system substantially reduced the environmental footprint of the stabilization step. Unlike conventional immersion methods requiring 50–100 mL of GA solution and generating hazardous liquid waste, the vapor-phase process operated with minimal reagent volume (≤0.5–10 mL) and eliminated contaminated wastewater production. This approach significantly reduced chemical consumption, minimized waste generation, and limited environmental release and operator exposure. Post-crosslinking washing and drying ensured removal of residual GA, as confirmed by cytocompatibility results. While GA use was not completely eliminated, its controlled vapor-phase application represents a reduced-impact crosslinking strategy aligned with green chemistry principles, particularly waste minimization and process intensification. Future studies will investigate fully bio-based crosslinkers such as genipin, citric acid, or enzymatic systems to further enhance the environmental profile of the platform.

Compared with many existing nanofiber-based wound dressings that rely on organic solvents, metal nanoparticles, or energy-intensive synthetic additives, the HC/PVA/CA system offers distinct advantages: (i) complete solvent-free aqueous electrospinning, (ii) incorporation of biodegradable and biocompatible natural polymers and botanical bioactives, (iii) multifunctional performance combining mechanical reinforcement, enhanced fibroblast activity, collagen stimulation, and antibacterial protection, and (iv) scalability through needleless electrospinning technology.

This work demonstrates that high biological functionality and environmentally conscious manufacturing can be integrated within a single nanofibrous wound dressing platform. The developed HC/PVA/CA membranes provide a sustainable and multifunctional alternative for advanced wound care, establishing a foundation for future in vivo validation, controlled release optimisation, long-term degradation studies, and industrial-scale green production strategies.

Acknowledgements The author also wishes to express her deepest gratitude to Mechanical Engineer Mr Bahaeddin Güner for his invaluable technical insights and continuous support throughout the development of this work.

Author contributions Elçin Tören: Conceptualisation, Methodology, Investigation, Writing original draft, Validation, Formal analysis, Visualisation, Project administration. Jakub Wiener: Supervise, validate, and write (review & editing).

Funding Open access publishing supported by the institutions participating in the CzechELib Transformative Agreement. The authors did not receive support from any organisation for the submitted work.

Data Availability Data obtained during the study are available from the corresponding author upon reasonable request.

Declarations

Competing interests The authors declare no competing interests.

Open Access This article is licensed under a Creative Commons Attribution 4.0 International License, which permits use, sharing, adaptation, distribution and reproduction in any medium or format, as long as you give appropriate credit to the original author(s) and the source, provide a link to the Creative Commons licence, and indicate if changes were made. The images or other third party material in this article are included in the article's Creative Commons licence, unless indicated otherwise in a credit line to the material. If material is not included in the article's Creative Commons licence and your intended use is not permitted by statutory regulation or exceeds the permitted use, you will need to obtain permission directly from the copyright holder. To view a copy of this licence, visit http://creativecommons.org/licenses/by/4.0/.

References

1. McGrath JA, Uitto J (2024) Structure and function of the skin. In: Griffiths CEM, Barker J,Bleiker TO, Hussain W, Simpson RC (eds) Rook's textbook of dermatology, 10th edn. Wiley-Blackwell, Oxford, pp 1–50
2. Lotfollahi Z (2024) The anatomy, physiology and function of all skin layers and the impact of ageing on the skin. Wound Pract Res 32. https://doi.org/10.33235/wpr.32.1.6-10
3. de Szalay S, Wertz P (2023) Protective barriers provided by the epidermis. Int J Mol Sci 24:3145. https://doi.org/10.3390/ijms24043145
4. Abdallah F, Mijouin L, Pichon C (2017) Skin immune landscape: inside and outside the organism. Mediators Inflamm 2017:5095293. https://doi.org/10.1155/2017/5095293
5. Wilkinson HN, Hardman MJ (2020) Wound healing: cellular mechanisms and pathological outcomes. Open Biol 10:200223. https://doi.org/10.1098/rsob.200223
6. Trinh X-T, Long N-V, Van Anh LT, Nga PT, Giang NN, Chien PN, Nam S-Y, Heo C-Y (2022) A comprehensive review of natural compounds for wound healing: Targeting bioactivity perspective. Int J Mol Sci 23:9573. https://doi.org/10.3390/ijms23179573
7. Bartold M, Ivanovski S (2025) Biological processes and factors involved in soft and hard tissue healing. Periodontol 2000 97:16–42. https://doi.org/10.1111/prd.12546
8. Sen CK, Gordillo GM, Roy S, Kirsner R, Lambert L, Hunt TK, Gottrup F, Gurtner GC, Longaker MT (2009) Human skin wounds: A major and snowballing threat to public health and the economy. Wound Repair Regen 17:763–771. https://doi.org/10.1111/j.1524-475X.2009.00543.x
9. Han G, Ceilley R (2017) Chronic wound healing: A review of current management and treatments. Adv Ther 34:599–610. https://doi.org/10.1007/s12325-017-0478-y
10. Rashdan HRM, El-Naggar ME (2023) Chap. 2 - Traditional and modern wound dressings—characteristics of ideal wound dressings. In: Khan R, Gowri S (eds) Antimicrobial Dressings. Academic Press, pp 21–42
11. Aderibigbe BA (2022) Hybrid-Based wound dressings: Combination of synthetic and biopolymers. Polym (Basel) 14:3806. https://doi.org/10.3390/polym14183806
12. Abrigo M, McArthur SL, Kingshott P (2014) Electrospun Nanofibers as Dressings for Chronic Wound Care: Advances, Challenges, and Future Prospects. Macromol Biosci 14:772–792. https://doi.org/10.1002/mabi.201300561
13. Saxena A, Anandhi RJ, Rashmi K, Singh N, Yadav D, Zabibah R (2024) Biomedical materials for sustainable wound care: A review of environmental impact and clinical efficacy. E3S Web Conferences 552. https://doi.org/10.1051/e3sconf/202455201060
14. Ahmad A, Ali U, Nazir A, Shahzad A, Khaliq Z, Qadir MB, Khan MA, Ali S, Aamir Hassan M, Abid S, Tahir R, Mushtaq B (2019) Toothed wheel needleless electrospinning: a versatile way to fabricate uniform and finer nanomembrane. J Mater Sci 54:13834–13847. https://doi.org/10.1007/s10853-019-03875-0
15. Khan MUA, Haider S, Raza MA, Shah SA, Razak SIA, Kadir MRA, Subhan F, Haider A (2021) Smart and pH-sensitive rGO/Arabinoxylan/chitosan composite for wound dressing: In-vitro drug delivery, antibacterial activity, and biological activities. Int J Biol Macromol 192:820–831. https://doi.org/10.1016/j.ijbiomac.2021.10.033
16. Ali M, Shanto P, Park M, Park I, Ibne Mahbub MS, Fahad MA, Farwa U, Lee B-T (2025) ZnO/curcumin nanobio-complex loaded bioactive multifunctional gelatin-PCL membranes for accelerated wound healing through enhanced angiogenesis. Biomaterials Adv 181:214631. https://doi.org/10.1016/j.bioadv.2025.214631
17. Augustine R, Kalarikkal N, Thomas S (2016) Electrospun PCL membranes incorporated with biosynthesized silver nanoparticles as antibacterial wound dressings. Appl Nanosci 6:337–344. https://doi.org/10.1007/s13204-015-0439-1
18. Gupta RK, Guha P, Srivastav PP (2024) Investigating the toxicological effects of nanomaterials in food packaging associated with human health and the environment. J Hazard Mater Lett 5:100125. https://doi.org/10.1016/j.hazl.2024.100125
19. Anegbe B, Ifijen IH, Maliki M, Uwidia IE, Aigbodion AI (2024) Graphene oxide synthesis and applications in emerging contaminant removal: a comprehensive review. Environ Sci Eur 36:15. https://doi.org/10.1186/s12302-023-00814-4
20. Hu Z-Y, Chang J, Guo F-F, Deng H-Y, Pan G-T, Li B-Y, Zhang Z-L (2020) The effects of dimethylformamide exposure on liver and kidney function in the elderly population. Med (Baltim) 99:e20749. https://doi.org/10.1097/MD.0000000000020749
21. Tahir R, Albargi HB, Ahmad A, Qadir MB, Khaliq Z, Nazir A, Khalid T, Batool M, Arshad SN, Jalalah M, Alsareii SA, Harraz FA (2023) Development of sustainable hydrophilic azadirachta indica loaded PVA nanomembranes for cosmetic facemask applications. Membranes 13:156. https://doi.org/10.3390/membranes13020156
22. Kwon M, Kim KS (2025) Nanofiber-based biomimetic platforms for chronic wound healing: Recent innovations and future directions. Tissue Eng Regen Med 22:755–770. https://doi.org/10.1007/s13770-025-00729-6
23. Al Hajj W, Salla M, Krayem M, Khaled S, Hassan HF, El Khatib S (2024) Hydrolyzed collagen: Exploring its applications in the food and beverage industries and assessing its impact on human health – A comprehensive review. Heliyon 10:e36433. https://doi.org/10.1016/j.heliyon.2024.e36433
24. Wakuda Y, Nishimoto S, Suye S, Fujita S (2018) Native collagen hydrogel nanofibres with anisotropic structure using core-shell electrospinning. Sci Rep 8:6248. https://doi.org/10.1038/s41598-018-24700-9
25. James JT, Dubery IA (2009) Pentacyclic triterpenoids from the medicinal herb, Centella asiatica (L.) Urban. Molecules 14:3922–3941. https://doi.org/10.3390/molecules14103922
26. Lee J, Jung E, Kim Y, Park J, Park J, Hong S, Kim J, Hyun C, Kim Y, Park D (2006) Asiaticoside induces human collagen i synthesis through TGFβ receptor I Kinase (TβRI Kinase)-independent smad signaling. Planta Med 72:324–328. https://doi.org/10.1055/s-2005-916227
27. Kavitha CV, Agarwal C, Agarwal R, Deep G (2011) Asiatic acid inhibits pro-angiogenic effects of VEGF and human gliomas in endothelial cell culture models. PLoS ONE 6:e22745. https://doi.org/10.1371/journal.pone.0022745
28. Mulat M, Banicod RJS, Tabassum N, Javaid A, Karthikeyan A, Jeong G-J, Kim Y-M, Jung W-K, Khan F (2025) Multiple strategies for the application of medicinal plant-derived bioactive compounds in controlling microbial biofilm and virulence properties. Antibiot (Basel) 14:555. https://doi.org/10.3390/antibiotics14060555
29. Nair A, Maity S, Pai V (2026) Sustainable extraction: a comprehensive review of advancements beyond conventional methods. Microchem J 220:116360. https://doi.org/10.1016/j.microc.2025.116360
30. Renkler Z, Cruz Maya I, Guarino V (2023) Optimization of polyvinyl alcohol-based electrospun fibers with bioactive or electroconductive phases for tissue-engineered scaffolds. Fibers 11:85. https://doi.org/10.3390/fib11100085
31. Tahir R, Jalalah M, Nazir A, Qadir MB, Khaliq Z, Bakht U, Faheem S, Ahmad A, Hareem F, Faisal M, Harraz FA (2024) Fabrication of sustainable, antioxidant, and antibacterial PVA nanomembranes loaded with plant extracts for dermal applications.

Mater Today Commun 39:109148. https://doi.org/10.1016/j.mtcomm.2024.109148
32. Rahman Khan MM, Rumon MMH (2025) Synthesis of PVA-based hydrogels for biomedical applications: Recent trends and advances. Gels 11:88. https://doi.org/10.3390/gels11020088
33. Nawaz A, Irshad S, Luo X, Qin Z, Walayat N, Khan MR, Tahir R, Akram N, Abdi G (2025) Electrospun PVA/alginate/cellulose nanofibers for probiotic delivery: fabrication, stability, and *in vitro* viability of probiotics. Carbohydr Polym Technol Appl 11:100938. https://doi.org/10.1016/j.carpta.2025.100938

Publisher's Note Springer Nature remains neutral with regard to jurisdictional claims in published maps and institutional affiliations.